



NAVAL POSTGRADUATE SCHOOL

MONTEREY, CALIFORNIA

THESIS

**DYNAMICS OF EASTERN BOUNDARY CURRENTS AND
THEIR EFFECTS ON SOUND SPEED STRUCTURE**

by

Vanessa M. Guthrie

June 2006

Thesis Co-Advisors:

Mary L. Batteen
John A. Colosi

Approved for public release; distribution is unlimited

THIS PAGE INTENTIONALLY LEFT BLANK

REPORT DOCUMENTATION PAGE			<i>Form Approved OMB No. 0704-0188</i>	
Public reporting burden for this collection of information is estimated to average 1 hour per response, including the time for reviewing instruction, searching existing data sources, gathering and maintaining the data needed, and completing and reviewing the collection of information. Send comments regarding this burden estimate or any other aspect of this collection of information, including suggestions for reducing this burden, to Washington headquarters Services, Directorate for Information Operations and Reports, 1215 Jefferson Davis Highway, Suite 1204, Arlington, VA 22202-4302, and to the Office of Management and Budget, Paperwork Reduction Project (0704-0188) Washington DC 20503.				
1. AGENCY USE ONLY (Leave blank)		2. REPORT DATE June 2006	3. REPORT TYPE AND DATES COVERED Master's Thesis	
4. TITLE AND SUBTITLE Dynamics of Eastern Boundary Currents and Their Effects on Sound Speed Structure			5. FUNDING NUMBERS	
6. AUTHOR(S) Vanessa M. Guthrie				
7. PERFORMING ORGANIZATION NAME(S) AND ADDRESS(ES) Naval Postgraduate School Monterey, CA 93943-5000			8. PERFORMING ORGANIZATION REPORT NUMBER	
9. SPONSORING /MONITORING AGENCY NAME(S) AND ADDRESS(ES) N/A			10. SPONSORING/MONITORING AGENCY REPORT NUMBER	
11. SUPPLEMENTARY NOTES The views expressed in this thesis are those of the author and do not reflect the official policy or position of the Department of Defense or the U.S. Government.				
12a. DISTRIBUTION / AVAILABILITY STATEMENT Approved for public release; distribution is unlimited			12b. DISTRIBUTION CODE	
13. ABSTRACT (maximum 200 words) Identifying the influence of eastern boundary current (EBC) dynamical processes on sound speed structure can provide better ocean models for acoustic predictions in littoral regions. This study will explore the effects of currents, wind and eddies on the sound speed structure of two different EBC models, the North Canary Current System (NCCS) and the Leeuwin Current System (LCS). These systems represent classical features of EBCs as well as regional anomalies. This study seeks to introduce sound speed analysis to the sigma coordinate primitive equation models and determine which regions of EBCs experience the largest changes in sound speed and most intense gradients. Results of model runs show that the dynamics of EBCs lead to large changes in sound speed and distort the vertical sound speed profile. The greatest change in sound speed in either region is caused by upwelling in the NCCS. Surface and associated subsurface eddies in the LCS are the largest scale feature in the study. The undercurrent of the NCCS and Meddies present the most intense (horizontal and vertical) gradients of sound speed change.				
14. SUBJECT TERMS Primitive Equation Model, Leeuwin Current System, North Canary Current System, Sigma-Level, Princeton Ocean Model (POM), Sound Speed, Eastern Boundary Current, Undersea Warfare			15. NUMBER OF PAGES 91	
			16. PRICE CODE	
17. SECURITY CLASSIFICATION OF REPORT Unclassified	18. SECURITY CLASSIFICATION OF THIS PAGE Unclassified	19. SECURITY CLASSIFICATION OF ABSTRACT Unclassified	20. LIMITATION OF ABSTRACT UL	

NSN 7540-01-280-5500

Standard Form 298 (Rev. 2-89)
Prescribed by ANSI Std. Z39-18

THIS PAGE INTENTIONALLY LEFT BLANK

Approved for public release; distribution is unlimited

**DYNAMICS OF EASTERN BOUNDARY CURRENTS AND THEIR EFFECTS
ON SOUND SPEED STRUCTURE**

Vanessa M. Guthrie
Ensign, United States Navy
B.S., United States Naval Academy, 2005

Submitted in partial fulfillment of the
requirements for the degree of

MASTER OF SCIENCE IN PHYSICAL OCEANOGRAPHY

from the

**NAVAL POSTGRADUATE SCHOOL
June 2006**

Author: Vanessa M. Guthrie

Approved by: Mary L. Batteen
Thesis Co-Advisor

John A. Colosi
Thesis Co-Advisor

Mary L. Batteen
Chair, Department of Oceanography

Donald P. Brutzman
Chair, Undersea Warfare Academic Committee

THIS PAGE INTENTIONALLY LEFT BLANK

ABSTRACT

Identifying the influence of eastern boundary current (EBC) dynamical processes on sound speed structure can provide better ocean models for acoustic predictions in littoral regions. This study will explore the effects of currents, wind and eddies on the sound speed structure of two different EBC models, the North Canary Current System (NCCS) and the Leeuwin Current System (LCS). These systems represent classical features of EBCs as well as regional anomalies. This study seeks to introduce sound speed analysis to the sigma coordinate primitive equation models and determine which regions of EBCs experience the largest changes in sound speed and most intense gradients. Results of model runs show that the dynamics of EBCs lead to large changes in sound speed and distort the vertical sound speed profile. The greatest change in sound speed in either region is caused by upwelling in the NCCS. Surface and associated subsurface eddies in the LCS are the largest scale feature in the study. The undercurrent of the NCCS and Meddies present the most intense (horizontal and vertical) gradients of sound speed change.

THIS PAGE INTENTIONALLY LEFT BLANK

TABLE OF CONTENTS

I.	INTRODUCTION.....	1
A.	NORTH CANARY CURRENT SYSTEM	1
B.	LEEUEWIN CURRENT SYSTEM.....	3
C.	EFFECTS ON SOUND SPEED.....	5
II.	MODEL DESCRIPTION.....	7
A.	DATA SETS	7
B.	PRE-PROCESSING	7
C.	BRIEF MODEL DESCRIPTION	9
D.	INITIALIZATION, FORCING AND BOUNDARY CONDITIONS.....	9
E.	SOUND SPEED CALCULATION.....	11
III.	RESULTS	13
A.	NORTH CANARY CURRENT SYSTEM MODEL	13
1.	Upwelling	13
2.	Undercurrent.....	14
3.	Meddies	14
4.	Filaments.....	14
5.	Classical and Unique Features.....	15
B.	LEEUEWIN CURRENT SYSTEM MODEL.....	16
1.	Leeuwin (Surface) Current	16
2.	Undercurrent.....	16
3.	Upwelling	17
4.	Eddies and Filaments.....	17
5.	Classical and Unique Features.....	18
C.	NCCS AND LCS COMPARISON	18
IV.	SUMMARY	21
	LIST OF REFERENCES.....	69
	INITIAL DISTRIBUTION LIST	75

THIS PAGE INTENTIONALLY LEFT BLANK

LIST OF FIGURES

Figure 1.	NCCS smoothed topography with depth in meters after applying a linear two-dimensional low-pass filter. (From: Sandwell and Smith (1996))	23
Figure 2.	LCS smoothed topography with depth in meters after applying a one-dimensional, iterative filter. Depth is in meters.	24
Figure 3.	NCCS wind stress vector and magnitude (in color) in Pascals calculated from annual climatological ECMWF winds (From: Trenberth et al., 1990)	25
Figure 4.	LCS annual average wind in m/s from climatological ECMWF winds obtained (From: Trenberth et al., 1990)	26
Figure 5.	NCCS, Surface temperature ($^{\circ}\text{C}$) and velocity vectors (cm/s) on day 1	27
Figure 6.	NCCS, Surface salinity (psu) and velocity vectors (cm/s) on day 1	28
Figure 7.	NCCS, Surface sound speed (m/s) and velocity vectors (cm/s) on day 1	29
Figure 8.	NCCS, Salinity (psu) cross-section at 36°N on day 1.	30
Figure 9.	NCCS, Salinity (psu) cross-section at 32.5°N on day 1.	31
Figure 10.	NCCS, Salinity (psu) cross-section at 39.3°N on day 1.	32
Figure 11.	NCCS, Sound speed (m/s) cross-section at 36°N on day 1.	33
Figure 12.	NCCS, Sound speed (m/s) cross-section 32.5°N on day 1.	34
Figure 13.	NCCS, Sound speed (m/s) cross-section 39.3°N on day 1.	35
Figure 14.	NCCS, Surface temperature ($^{\circ}\text{C}$) and velocity vectors (cm/s) on day 20	36
Figure 15.	NCCS, Difference in sound speed (m/s) from initial conditions, cross-section at 39.3°N on day 20.	37
Figure 16.	NCCS, Surface temperature ($^{\circ}\text{C}$) and velocity vectors (cm/s) on day 63	38
Figure 17.	NCCS, Difference in sound speed (m/s) from initial conditions, cross-section at 39.3°N on day 63.	39
Figure 18.	NCCS, Difference in sound speed (m/s) from initial conditions, cross-section at 36°N on day 63.	40
Figure 19.	NCCS, Difference in sound speed (m/s) from initial conditions, cross-section at 32.5°N on day 63.	41
Figure 20.	NCCS, Difference in sound speed (m/s) from initial conditions, cross-section at 32.5°N on day 36.	42
Figure 21.	NCCS, Difference in sound speed (m/s) from initial conditions, cross-section at 36°N on day 36.	43
Figure 22.	NCCS, Difference in sound speed (m/s) from initial conditions, cross-section at 39.3°N on day 36.	44
Figure 23.	NCCS, Temperature ($^{\circ}\text{C}$) and velocity (cm/s) at 1200 m depth on day 45.	45
Figure 24.	NCCS, Difference in sound speed (m/s) from initial conditions, cross-section at 39.3°N on day 45.	46
Figure 25.	NCCS, Difference in sound speed (m/s) from initial conditions, cross-section at 32°N on day 63.	47
Figure 26.	NCCS, Difference in sound speed (m/s) from initial conditions, cross-section at 33.9°N on day 63.	48
Figure 27.	LCS, Initial conditions of surface salinity (psu).	49
Figure 28.	LCS, Initial conditions of surface temperature ($^{\circ}\text{C}$).	50

Figure 29.	LCS, Initial conditions of surface sound speed (m/s).....	51
Figure 30.	LCS, Sound speed (m/s) cross-section at 28°S for initial conditions.	52
Figure 31.	LCS, Surface sound speed (m/s) and velocity vectors (cm/s) on day 20.....	53
Figure 32.	LCS, Difference in sound speed (m/s) from initial conditions, cross-section at 33.5°S on day 20.....	54
Figure 33.	LCS, Surface sound speed (m/s) and velocity vectors (cm/s) on day 36.....	55
Figure 34.	LCS, Difference in sound speed (m/s) from initial conditions, cross-section at 33.5°S on day 36.....	56
Figure 35.	LCS, Difference in sound speed (m/s) from initial conditions, cross-section at 33.5°S on day 20.....	57
Figure 36.	LCS, Surface temperature (°C) and velocity vectors (cm/s) on day 20.....	58
Figure 37.	LCS, Surface sound speed (m/s) and velocity vectors on day 45.....	59
Figure 38.	LCS, Difference in sound speed (m/s) from initial conditions, cross-section at 28°S on day 45.....	60
Figure 39.	LCS, Difference in sound speed (m/s) from initial conditions, cross-section at 28°S on day 63.....	61
Figure 40.	LCS, Difference in sound speed (m/s) from initial conditions, cross-section at 35.5°S on day 45.....	62
Figure 41.	LCS, Surface sound speed (m/s) on day 54.....	63
Figure 42.	LCS, Difference in sound speed (m/s) from initial conditions, cross-section at 33.5°S on day 54.....	64

LIST OF TABLES

Table 1.	Vertical levels and depths used by Levitus and Boyer (1994) and Levitus et al. (1994).	65
Table 2.	Values of sigma levels for NCCS and LCS models.	65
Table 3.	Impact of features on sound in the NCCS.	66
Table 4.	Impact of features on sound in the LCS.....	67

THIS PAGE INTENTIONALLY LEFT BLANK

ACKNOWLEDGMENTS

I would like to thank my advisors, Professor Mary Batteen and Professor John Colosi, for their unending patience and assistance with this study. Their guidance has made my education at NPS exceptional and purposeful. My appreciation is immeasurable. I would also like to thank CDR Tony Miller for the countless hours spent explaining this project, from model to code to analysis. His advice has been invaluable and I could not have completed the study without his help. Thank you to Team Ensign and the others who struggled together through the year. Most importantly, I would like to thank my family for their incredible support at every milestone in my life.

THIS PAGE INTENTIONALLY LEFT BLANK

I. INTRODUCTION

As Navy operations continue to move into coastal regions, the need for accurate predictions of shallow water acoustics is of particular importance. Sound speed structure in “blue water” has been studied for many years and reasonable models exist to predict large scale and small scale sound speed variability. However, the complex ocean dynamics of littoral regions complicate the study of acoustics near the coast. Identifying the influence of dynamical processes like upwelling, shelf eddies, filaments, meanders, etc., on sound speed structure can provide better ocean models for acoustic predictions in littoral regions.

This study will explore the effects of currents, wind and eddies on the sound speed structure of two different eastern boundary current (EBC) regions. The EBCs of specific interest are the North Canary Current System (NCCS) off Morocco and the Iberian Peninsula, and the Leeuwin Current System (LCS) off Western Australia. These systems represent classical features of EBCs as well as regional anomalies. Major subtropical EBCs such as the California, Peru, and Benguela Currents are wind-driven and characterized by climatologically weak (<10 cm/s), broad (~ 1000 km wide), cold surface flow towards the equator. Surface currents flow in the direction of the prevailing winds with a poleward undercurrent below. The EBC thermocline is typically shallow (<30 m depth) and the region has high biological production due to vast regional upwelling (Parrish et al., 1983). While the NCCS and LCS contain a number of these classical features, both regions include notable anomalies.

A. NORTH CANARY CURRENT SYSTEM

The NCCS stretches from $\sim 10^{\circ}\text{N}$ to $\sim 45^{\circ}\text{N}$ along the coast of northwestern Africa and the Iberian Peninsula. This system is considered a classical EBC and marks the closing eastern boundary of the North Atlantic Gyre. Typical of other EBCs, the mean equatorward Canary Current (CC) is a relatively broad (~ 1000 km), slow (~ 10 - 30 cm/s), yearlong surface flow extending from depths of ~ 500 m (Wooster and Reid, 1976). A poleward undercurrent exists near the coast beneath the CC and is relatively narrow

(~10–40 km) and weak (~2-10 cm/s). The undercurrent is strongest between depths of ~100 m and ~600 m, varying with season and latitude. In winter, the CC shoals to the north near Cabo da Roca and forms a component commonly referred to as the Iberian Current (IC) (Haynes and Barton, 1990). The IC is a relatively narrow (~25-40 km), weak (~20-30 cm/s), seasonal current found trapped near the coast against the shelf break (Fiuza, 1980; Frouin et al., 1990; Haynes and Barton 1990).

The NCCS is predominately influenced by equatorward, upwelling favorable winds produced by the Azores High. The Azores High is a semi-permanent subtropical high pressure system located in the northeastern Atlantic Ocean, similar in nature and behavior to the North Pacific Subtropical High (Nelson, 1977). The center of the high migrates meridionally with the seasons, causing wind stress values over the NCCS to vary temporally.

Observations of the sea surface in the NCCS region have shown highly energetic mesoscale features, including jet-like surface currents, meanders, eddies and filaments. Satellite sea surface images have shown nearshore upwelling during periods of upwelling favorable winds with several narrow filaments of cooler water extending off the coast of the Iberian Peninsula (Fiuza and Sousa, 1989) and Cape Ghir in northwest Africa (Van Camp et al., 1991; Hagen et al, 1996). In these images, upwelling filaments often extend ~80-150 km offshore with alongshore spacing of ~80-100 km between filaments (Haynes et al., 1993), and terminate with dipole eddy pairs (Fiuza et al., 1982; Barton, 1998). Observations have also shown anti-cyclonic and cyclonic pairs of mesoscale eddies on the order of 100 km off the coast of the Iberian Peninsula (Fiuza, 1984; Stammer et al., 1991). These mesoscale features have been observed during periods of upwelling-favorable winds and are located near coastline irregularities such as capes. These observations provide evidence that wind forcing along with coastline irregularities appear to be important mechanisms in the formation and continuance of many of the mesoscale features found in the NCCS domain and other EBC regions (Batteen et al., 2000).

A unique feature that distinguishes the NCCS from other classical EBCs is the influence of the Mediterranean Outflow (MO). Due to its high density, the MO flows down the continental slope in the Gulf of Cadiz as a narrow gravity current and entrains

the less dense North Atlantic Central Water. Coriolis acceleration causes the outflow to deflect to the right as it leaves the strait (Bower et al., 1997). The highly saline plume of the MO dilutes, thickens, and becomes vertically differentiated into two distinct cores as it follows the northern rim of the Gulf of Cadiz (Iorga and Lozier, 1999; Bower et al., 1997). At $\sim 7^{\circ}\text{W}$ in the Gulf of Cadiz, the two cores exist at depths of $\sim 600\text{-}900\text{ m}$ and $\sim 1100\text{-}1200\text{ m}$. Both cores continue to flow westward along the southern coast of Spain and turn poleward around Cabo de Sao Vicente (Amber and Howe, 1979; Iorga and Lozier, 1999). A third, shallower, poleward core of Mediterranean water has also been traced from the Strait of Gibraltar northward to $\sim 38.5^{\circ}\text{N}$ off western Portugal (Amber, 1983). Additionally, climatological cyclonic circulation in the southwestern Gulf of Cadiz spreads the salty MO south $\sim 34^{\circ}\text{N}$ (Iorga and Lozier, 1999).

In the past three decades, studies on how the Mediterranean salt tongue is maintained have prompted a search within the region for submesoscale coherent vortices (SVCs) or Meddies (e.g., Armi et al., 1989). Observations reveal that Meddies are lenslike features, containing a core of Mediterranean waters $200\text{-}1000\text{ m}$ thick centered at about 1000 m , which are less stratified than the surrounding fluid. They are typically $20\text{-}100\text{ km}$ in diameter and have temperature and salinity anomalies of approximately 2°C and 1 psu . This density structure supports an energetic anti-cyclonic rotation with peak azimuthal velocities of about 30 cm/s and rotation periods of $2\text{-}7$ days (Armi et al., 1989; Hebert et al., 1990). The primary generation region of Meddies is widely accepted to be near Cabo de Sao Vicente off southwest Portugal. Several different trajectories of Meddies have been observed, including a southwestward movement into the Canary Basin, and westward translations south of the Azores (Richardson and Tychensky, 1998).

B. LEEUWIN CURRENT SYSTEM

The Leeuwin Current system is a sharp contrast to the typical EBC equatorward surface currents and poleward undercurrents of the NCCS. The Leeuwin Current is an anomalous, surface EBC off the coast of Western Australia that flows poleward along the continental shelf ($\sim 200\text{ m}$ depth) from Shark Bay to Cape Leeuwin. At the cape, it swings eastward as far as the Great Australian Bight (Cresswell and Golding, 1980). Like the NCCS region, prevailing winds along the coast of Western Australia are

predominantly equatorward. Unlike the NCCS, the Leeuwin Current is driven by an uncharacteristically large thermohaline gradient that overwhelms the winds stress. There is general agreement (Godfrey and Ridgway, 1985) that the LCS is generated by a meridional pressure gradient resulting from excessive heating in the equatorial region and large amounts of cooling in the poleward region. The source for the Leeuwin Current is predominantly an alongshore steric height gradient due to tropical Pacific water from the Indonesian throughflow (Godfrey and Ridgway, 1985; Hirst and Godfrey, 1993) and is augmented by a source from the North West Shelf (e.g., Gentili, 1972), possibly having its origin in the Pacific Ocean (Hirst and Godfrey, 1993). As a result of this strong inflow of subtropical waters towards the coast, the LCS intensifies poleward (Batteen et al., 1992).

Observations off the coast of Western Australia have shown the LCS is a strong (>150 cm/s at times), narrow (<100 km wide), poleward surface current that opposes the prevailing wind direction (Godfrey and Ridgway, 1985; Cresswell and Golding, 1980; Godfrey et al., 1986). Associated with the system are near-surface isopycnals that slope downward, surface dynamic height fields that increase toward the coast, and an equatorward undercurrent (Thompson, 1984; McCreary et al., 1986). Additionally, the LCS contains anomalous warm water at the surface and a deep (>50 m depth) thermocline (Thompson, 1984). The warm flow is credited with the appearance of tropical marine species off both the western and southwestern Australian coasts (Pearce and Griffiths, 1991) and lower biological production due to vast regions of downwelling (Batteen et al., 1992).

Below the Leeuwin Current is an anomalous equatorward undercurrent (e.g., Church et al., 1998). Current meter data from the Leeuwin Current Interdisciplinary Experiment (LUCIE) showed the undercurrent to be narrow and confined to the continental slope between ~ 250 m and 450 m depth (Smith et al., 1991). Between ~ 250 m and 350 m depth, the undercurrent can attain speeds comparable to the surface flow, exceeding on average 10 cm/s, up to ~ 30 cm/s (Smith et al. 1991). Although there is evidence of a 20 cm/s westward flow centered between ~ 400 m and 700 m depth off the southern coast ($\sim 116^\circ\text{E}$), no studies to date have clearly resolved whether there is a westward undercurrent off Southern Australia (Cresswell and Peterson, 1993).

From February to May each year, the Leeuwin Current strengthens considerably and strong eddies develop. Other dynamical features that have been observed in the LCS are offshoots of the current, meanders and both anticyclonic and cyclonic eddies (e.g., Legeckis and Cresswell, 1981).

C. EFFECTS ON SOUND SPEED

Sound speed profiles may be varied by a number of local conditions. Features such as internal waves, eddies or tides create variations in water density with depth (vertical displacement of the ocean layers). Near polar regions or river estuaries, profiles are affected by horizontal advection of water masses (Lurton, 2002). The classical and unique features of the NCCS and LCS change sound speed through both processes, vertical displacement or horizontal advection. Surface and subsurface eddies in both regions impact sound speed by their vertical displacements. Upwelling is another form of vertical displacement where deep water masses are lifted to the upper ocean. The anomalous surface current of the LCS advects warm water along the coast, causing intense horizontal gradients of sound speed. Mediterranean waters exiting the Strait of Gibraltar into the North-East Atlantic is a classic example of water mass exchange and horizontal advection (Lurton, 2002). Through these processes, the features of both regions will affect sound speed.

Previous numerical studies by Batteen et al. (2006) investigated the effects of annual climatological wind forcing, initialized thermohaline gradients, and topography on the Leeuwin Current system. Similar studies have been conducted for the NCCS region, investigating the roles of wind forcing, bottom topography and thermohaline gradients on classical as well as unique features of the Northern Canary Current system (Martinho, 2001). This study seeks to extend prior efforts in these areas by introducing sound speed analysis. The analysis will determine which regions of EBCs experience the largest changes in sound speed and most intense gradients. A comparison of the NCCS and LCS region will provide a diverse compilation of classical and unique features and their effects on sound speed. Knowledge gained from this study will allow Navy oceanographers to better understand the complex ocean dynamics observed in EBCs and

more accurately predict sound speed variability in these regions. In turn, the Undersea Warfare (USW) community will be better equipped to support submarine operations in these areas.

II. MODEL DESCRIPTION

A. DATA SETS

The model was initialized using annual climatological temperature and salinity maps obtained from Levitus and Boyer (1994) and Levitus et al. (1994). These data sets use a 1 by 1 degree horizontal resolution at thirty-three vertical levels shown in Table 1.

Topographic data was obtained from the Institute of Geophysics and Planetary Physics, University of California San Diego (Sandwell and Smith, 1996). The bottom topography has a resolution of 2 minutes (1/30 of a degree) and was compiled from 30 years of bottom echo soundings by ships. Gravity data was used to estimate soundings in the vast regions in which there was sparse or no ship data.

Climatological wind fields were obtained from the European Centre for Medium Range Weather Forecasts (ECMWF) near-surface wind analyses (Trenberth et al., 1990). The wind data uses a 2.5 by 2.5 degree grid.

B. PRE-PROCESSING

The original topography was interpolated to the resolution of the POM model for each current system. In the NCCS model, the resolution was 3 by 3.7 km in the shallow regions and 6 by 7.4 km in deeper region, resulting in a total 287 by 241 horizontal grid. The variable grid in this model allows the use of more (less) points in regions of large (small) gradients. The highest resolution was used where the values of the slope parameter (defined by Mellor et al., 1998, as $\frac{|\delta H|}{2 * \bar{H}}$, where \bar{H} is the average depth and δH is the difference in depth between two adjacent cells) were the largest in both the latitude and longitude directions. The maximum suggested slope parameter to be used in sigma coordinate models is 0.2 (Mellor, 1996). Since the slope parameter was greater than this maximum value over much of the area, the topography was smoothed with a linear, 2D low-pass filter in order to meet this criterion. The new depth of each point calculated with this filter was a non-weighted average of 15 by 15 points surrounding the

point. Depths greater than 2500 m were reassigned to the maximum depth of 2500 m. Land was assigned a depth of 10 m to avoid division by zero in the model and the Strait of Gibraltar was closed (Figure 1).

Similarly, the LCS model horizontal grid resolution varies from 5.7 km by 6 km to 13.7 km by 10.2 km, resulting in 298 by 233 points. The finest resolution, 5.7 km by 6 km, was located over the continental shelf and slope around the southwest corner of Australia; the bottom slope and temperature gradient were greatest in this area. Original topography was smoothed with a one dimensional (1D), iterative method (Martinho and Batteen, 2006). This filtering process has been shown to satisfy the slope criterion while maintaining coastline irregularities, continental shelves, and relative maxima such as seamounts and islands. To avoid altering slope parameters after they have been adjusted, a two dimensional (2D) averaging filter was first applied to the coastline. For the topography, the signed slope parameter was then calculated along each grid line in one, initial direction over the domain. Any two adjacent cells with a slope parameter greater than the limit were adjusted to the limit value, and the line was recalculated. When all grid lines in the initial direction were adjusted, the topography matrix was rotated 90 degrees. Each process was repeated until the topography was adjusted for all directions (rotated 360°). To avoid division by zero in the model, land was assigned a depth of 20 m and depths greater than 2500m were reassigned to 2500 m (Figure 2).

In both models, the annual climatological temperature and salinity values were interpolated for the horizontal spatial resolution of the model and for the 21 vertical sigma levels with a three dimensional (3D) linear interpolation scheme. Daily seasonal winds were averaged over time in order to obtain the annual, non-weighted, average wind vector field. The wind vectors were also interpolated for the horizontal spatial resolution of the model with a two dimensional linear interpolation scheme. Since wind stress rather than the wind forces the model, the annual wind vectors were then used to compute the wind stress.

C. BRIEF MODEL DESCRIPTION

The Princeton Ocean Model (POM) was used in the model studies of the NCCS and LCS. The POM, a well-documented model, is a primitive equation, free surface model with a second-moment turbulence closure scheme (Mellor and Yamada, 1982). Using bottom-following sigma levels, the POM can realistically simulate processes associated with continental shelf flows and bottom boundary layer dynamics in local domains such as bays, estuaries and coastal regions. This model utilizes 21 vertical sigma levels. The sigma values ranged from zero at the surface to minus one at the bottom with the vertical grid spacing proportional to the ocean depth. The vertical resolution was higher near the surface and the bottom in order to resolve the boundary layers in these regions. An implicit vertical time differencing scheme was used to eliminate the time constraint of the vertical grid near the surface, bottom and in shallow water. The sigma values for both models are found in Table 2.

The prognostic variables of the model are potential temperature, salinity, density, three velocity components, surface elevation, turbulent kinetic energy and length scale. The model has a split time step interval for external and internal modes. The external mode solves the equations for the vertically integrated momentum equations. It also provides the sea surface and barotropic velocity components and has a time step of six seconds. The internal mode solves the complete 3D equations and has a time step of 300 seconds in the LCS model and 180 seconds in the NCCS model.

A Smagorinsky formulation (Smagorinsky et al., 1965) was used for the horizontal diffusion in which the horizontal viscosity coefficients depend on the grid size, the velocity gradients and a coefficient. Consistent with other POM studies, a value of 0.2 was assigned to this coefficient (Ezer and Mellor, 1997).

D. INITIALIZATION, FORCING AND BOUNDARY CONDITIONS

The model was initialized with annual temperature and salinity values obtained from Levitus and Boyer (1994) and Levitus et al. (1994). Since the model runs reached a quasi-equilibrium state in a relatively short time (<60 days), zero salinity and temperature fluxes have been prescribed at the ocean surface.

The model was forced from rest with the annual ECMWF wind fields which were interpolated for the model grid. In the NCCS region, the wind stress is stronger in the southern region of the domain and weaker off Iberia and in the Gulf of Cadiz (Figure 3). In the LCS region, westerly winds dominate the southern portion of the domain (Figure 4). Along the west coast of Australia the winds are southerly to south-southeasterly and generally increase in strength away from the coast.

Correct specification of the open boundary conditions (BCs) is very important to achieving realistic results without reflections, clamping, spurious currents or numerical alteration of the total volume of water in the model. Generally, boundary conditions are specific to each model and study. For models with a free surface, such as the two used here, BCs should be transparent to the waves. A gradient boundary condition (Chapman, 1985), which allows geostrophic flow normal to the boundary, works best for the elevation. For baroclinic velocity components normal to the boundary, an explicit wave radiation scheme based on the Sommerfeld radiation condition was used. For inflow situations, the model was forced with annual temperature and salinity values obtained from Levitus and Boyer (1994) and Levitus et al. (1994), while an advection scheme was used in outflow situations. An improvement on previous models is the introduction of an advanced volume constraint subroutine based on research performed by Marchesiello et al. (2001), which drastically reduced the loss of volume at the boundaries to insignificant levels.

For the barotropic velocity components, a Flather radiation plus Roed local solution (FRO) was used. Palma and Matano (2000) showed good results with the FRO during BC tests to determine the BCs response to an alongshelf wind stress. Palma and Matano (1998) also showed that the FRO BC had good reflection properties and results in a test that determined the BC response to the combined action of wind forcing and wave radiation. These tests were executed with the barotropic version of POM and compared with benchmark results (no boundary conditions).

E. SOUND SPEED CALCULATION

Sound speed in this study was calculated using the Chen and Millero equation in the UNESCO algorithm (Fofonoff and Millard, 1983), and is a function of temperature, salinity, and pressure (depth and latitude). Equations for the speed of sound in seawater based on laboratory measurements have been published by Wilson (1960), Del Grosso (1974) and Chen and Millero (1977). The equation of Chen and Millero is generally accepted as the sound speed standard, although there is much debate in scientific literature about the accuracy and range of applicability of these equations. Studies have shown the difference between Del Grosso and Chen and Millero sound speed calculations increases with depth to almost 0.6 m/s at 5000 dbar for realistic ocean temperatures and salinities (Dushaw et al., 1993). Since the models in this study extend to 2500 m depth, the Chen and Millero equation was selected. Depth was converted to pressure by the Saunders (1981) depth-to-pressure conversion technique.

THIS PAGE INTENTIONALLY LEFT BLANK

III. RESULTS

A. NORTH CANARY CURRENT SYSTEM MODEL

Initial climatology of the NCCS region can be seen in Figure 5 and Figure 6. Temperature and salinity decrease roughly linearly from north to south by 3°C and 0.8 psu, respectively. Surface sound speed (Figure 7) increases by ~ 5 m/s from north to south and is relatively homogeneous, with the exception of waters north of 37°N which resemble the temperature gradient. A cross-sectional profile of salinity at day 1 through the gulf at 36°N (Figure 8) shows the Mediterranean Outflow (MO) signature at ~ 1200 m depth with values of ~ 36.2 psu, and characteristically high salinity values of the North Atlantic waters in the upper 300 m. Evidence of the outflow waters can be seen across the entire region (not shown), although the highest values of salinity are found in the gulf. Cross-sections of salinity at 32.5°N (Figure 9) and 39.3°N (Figure 10) show that values at depths of the MO decrease by ~ 0.4 psu to the south and ~ 0.1 psu to the north of the gulf (compare Figures 8, 9, and 10). The MO signature appears in sound speed profiles for the same day and latitudes (Figure 11), creating two distinct sound channels at depths of approximately 500 m and 2000 m. This particular profile is unique to this region where the warm, salty waters of the Mediterranean mix with the North Atlantic. Important acoustically, the double minimum features are strongest in the gulf and decrease towards the north and south, exemplifying the same spreading of the Mediterranean waters seen in salinity cross sections (Figures 11, 12 and 13).

1. Upwelling

Using these initial conditions and the winds, the model was run for 90 days. By day 20, upwelling is evident along the coast (Figure 14). Cross sections profiling the difference in sound speed from the initial conditions indicate a decrease over time in sound speed caused by the cooler waters. For example, the effect on sound structure at latitude 39.3°N (Figure 15) has decreased ~ 15 m/s. The upwelling extent continues to broaden along the entire coastline through day 45 and reaches its maximum extension by day 63 (Figure 16). This wide and shallow feature subsequently decreases sound speed along the shelf by a maximum of ~ 19 m/s at all latitudes from the surface to ~ 200 m depth in the north (Figure 17), ~ 400 m depth in the gulf (Figure 18), and ~ 500 m depth in

the south (Figure 19). Although upwelling primarily impacts the mixed layer, the horizontal gradient of sound speed in the upper layer is not large and is changing ~ 19 m/s over ~ 280 km.

2. Undercurrent

A warm, poleward undercurrent appears by day 20 north of the Gulf of Cadiz. The undercurrent reaches its maximum intensity by day 36, after which eddies and Meddies begin to form and spin off. South of the gulf, the sound speed increases by 5 m/s due to the warm waters of the undercurrent flowing northward (Figure 20). Similarly, cross sections within the gulf (36°N) also show a 5 m/s increase (Figure 21). North of this latitude, the undercurrent advects MO waters and has a greater effect on sound speed structure. A cross section of sound speed difference at 39.3°N shows a 9 m/s increase due to the added salinity of the MO to the warm undercurrent (Figure 22). These changes in sound speed occur over a shorter longitudinal distance than upwelling, extending ~ 15 km from the point of maximum increase to the point of no change in sound speed. The resulting horizontal gradient of sound at depth along the slope is significantly larger than in the mixed layer.

3. Meddies

In the undercurrent around Cabo Roca (39.3°N), a Meddy forms by day 45, generating a dipole pair (Figure 23). Sound speed across the Meddy increases by ~ 6 m/s within 50 km horizontally and 600 m vertically (Figure 24). As the Meddy mixes MO waters with the North Atlantic, its effect on sound speed weakens and the gradients become less condensed. By day 63, the Meddy and dipole pair are still visible in the 39.3°N cross section, but show only a 3.5 m/s increase over 50 km (Figure 17). To the south, an eddy appears in the undercurrent at 32°N by day 63; however, this eddy forms after the undercurrent has been established and the MO waters have already been advected to the north. Consequently, this eddy does not contain the MO signature and so is not considered a Meddy. Without the added salinity of the MO, the sound speed increases only ~ 2 m/s across the ~ 100 km feature (Figure 25).

4. Filaments

On the surface, the NCCS generates several filaments of cooler water from upwelling. By day 63, a topographic feature at 33.9°N causes a surface eddy to spin off

from these filaments. The well-defined, cold-core eddy causes a decrease in sound speed of ~ 12.5 m/s across ~ 40 km and reaches below the mixed layer to a depth of 1500 m (Figure 26). Similar to the undercurrent eddy at 32°N , this eddy is not influenced by the MO, despite affecting depths deeper than the outflow.

5. Classical and Unique Features

The NCCS was chosen for this study for its classical upwelling and equatorward surface current as well as the unique impact of the Mediterranean Outflow. Table 3 summarizes the effects on sound speed by each feature in this region. Results are interpreted in terms of effective change in sound speed from initial conditions as well as spatial extent. Of critical acoustical importance are the spatial gradients of sound speed caused by these features.

In the NCCS, upwelling clearly incurs the greatest change on sound speed, affecting a large surface area through the mixed layer. Sound speed fluctuation in this feature is driven by the change in temperature and reaches a maximum at the coast soon after the appearance of upwelling, remaining constant while upwelling extent continues to grow steadily. As expected, upwelled waters are significantly cooler than initial surface conditions and cause a decrease in sound speed. Consequently, eddies which spin off upwelling filaments also cause a large decrease in sound speed. These mesoscale surface eddies are significant acoustical features due to their large gradients of sound speed. Although the surface eddy affects sound speed ~ 6.5 m/s less than upwelling, sound speed structure in the eddy changes over a much shorter longitudinal distance, leading to larger gradients.

Effects of Mediterranean waters in the NCCS model can be seen in results of the northward undercurrent. Within the Gulf of Cadiz and south of the gulf, the undercurrent incurs a consistent change, primarily due to the increase in temperature from southern waters. Although the undercurrent narrows to the north, its influence on sound speed increases due to the added salinity of the MO advected northward in the current. Similar results are seen in a comparison of the undercurrent eddy and Meddy. The eddy found near the south boundary of the domain causes very little change to the sound speed structure. The size of the Meddy off Cabo da Roca is on the same order as the undercurrent eddy; however, the Meddy contains the MO signature. Consequently, the

Meddy incurs a greater sound speed change. The NCCS model shows the Meddy dissipating over time; however, Meddies in the North Atlantic play a fundamental role in maintaining the large-scale salt tongue and gradual decrease in salinity is expected (Bower et al., 1997). Whereas temperature is a foremost factor affecting sound speed, the NCCS represents a region uniquely affected by salinity.

B. LEEUWIN CURRENT SYSTEM MODEL

Figures 27, 28, and 29 show the initial climatology for the LCS model. The meridional temperature gradient of this region (Figure 28) is notably larger than the NCCS region with a maximum temperature near Shark Bay of $\sim 24^{\circ}\text{C}$ and a minimum of 14°C at the southern edge of the model domain. The climatological surface salinity (Figure 27) shows a maximum of ~ 38.9 psu at the center of the western edge of the model domain and a minimum of ~ 35.3 psu along the northern Australian coast. Despite a slight increase in salinity between 34°S and 30°S (Figure 27), the surface sound speed decreases roughly uniformly from north to south. The resulting difference between maximum and minimum surface sound speed is ~ 8 m/s (Figure 29). Cross-sectional profiles of sound at various latitudes (e.g., 28°S shown in Figure 30) indicate a minimum of ~ 1490 to 1494 m/s over the entire region at ~ 1200 m depth.

1. Leeuwin (Surface) Current

By day 20, the narrow (~ 90 km) Leeuwin Current has formed primarily as a result of the thermal gradient over the region (Figure 31). Warm water is advected poleward within the narrow flow, resulting in large temperature gradients around Cape Leeuwin. Figure 32 shows large horizontal and vertical gradients across this feature with an increase of ~ 9 m/s. The current quickly strengthens over time and, by day 36, has reached a width of ~ 160 km notably without the formation of eddies (Figure 33). Sound speed increases by ~ 12 m/s (Figure 34). After day 36, the current reduces in intensity and eddy generation begins.

2. Undercurrent

Similar to the surface current, an equatorward undercurrent appears around Cape Leeuwin by day 20 (Figure 35). By day 36, the undercurrent appears at all latitudes on the west coast (not shown) and has reached its maximum intensity without the formation

of eddies. Unlike the wide, offshore surface current, the undercurrent narrows considerably from ~ 90 km horizontally and 1000 m vertically to ~ 25 km and 500 m as it flows equatorward. Topography traps the current to the shelf at ~ 1200 m depth. Consequently, this feature primarily affects the shelf break region, resulting in a ~ 3 m/s to 7 m/s decrease in sound speed.

3. Upwelling

Although the surface current flows opposite to the wind direction, southerly winds generate minimal upwelling predominantly in the bight around 33.5°S and between 28°S and 30°S (Figure 36). Note that upwelling does not appear where the LCS flows close to the coast. In the regions that are affected by upwelling, water relatively cooler than the surface current appears by day 20; however, a cross section of the bight shows almost no change from the initial sound structure on the shelf (Figure 32). Due to the shallow depth of the shelf and the warm water advected by the LCS from the north, upwelled waters cause either no change or a slight increase from sound speed initial conditions. Upwelling reaches a maximum extent at day 63 and increases sound speed by 1 m/s in the north (28°) and 4 m/s in the bight. The waters are confined to the shelf, extending 40 km to 70 km from the coast and from the surface to 100 m depth.

4. Eddies and Filaments

Strong eddies are among the most notable features of this model run. By day 36, baroclinic instability generated by increasing vertical shear causes the current to meander (Figure 33). By day 45, meanders at 28°S and 35.5°S become warm-core eddies propagating westward (Figure 37). Cross sections at 28°S (Figures 38 and 39) show that the eddies grow to ~ 250 km in width from day 45 to day 63 and affects the upper 1500 m of the water column by ~ 7 m/s. Note that no mesoscale features in the undercurrent form at this latitude. At 35.5°S , smaller (~ 130 km) eddies spin off of Cape Leeuwin with warm-core eddies at the surface and cold-core eddies in the undercurrent (Figure 40). Unlike the surface eddy at 28°S , this warm-over-cold core eddy affects the entire water column, increasing the upper 1200 m by a maximum ~ 7 m/s and decreasing the lower 1300 m by 5 m/s. Equatorward winds around the cape help to develop eddy dipole pairs which propagate westward. The third and strongest eddy forms by day 54 at 33.5°S , also as a result of opposing winds and topography (Figure 41). Unlike eddies off the southern

coast of Australia, this ~ 180 km feature does not propagate westward and only affects the water column to ~ 400 m depth. The warm core is more defined than previously formed eddies and produces a strong sound speed gradient across ~ 90 km (Figure 42). This surface and undercurrent eddy causes a ~ 10 m/s increase and ~ 2 m/s decrease respectively in sound speed.

5. Classical and Unique Features

Table 4 summaries the results of the LCS model run and details the impact of each feature on sound speed. The strong meridional pressure gradient off the coast of Australia produces features unique to the LCS region, particularly the surface current. This feature incurs the greatest change in sound speed due to poleward advection of warm waters. Consequently, sound speed increases within the current and the greatest change from initial conditions occurs in the coolest waters around Cape Leeuwin. The surface current tapers towards the cape, creating a narrow, shallow feature with a large effect on sound speed. Similarly, the undercurrent advects cooler water and narrows as it flows northward, causing a region of decreasing sound speed between 1000 m and 1400 m depth. Both the surface and undercurrent remain close to the topography. Eddies in the surface current and in the undercurrent tend to form off the same topographic features, causing changes in the sound speed of the entire water column. These eddies are significant influences on sound speed structure as they affect large, isolated volumes of the domain by as much as 10 m/s.

In the LCS, forcing from the thermal gradient overwhelms wind stress. Upwelling is confined to the latitudes where the current has drifted westward away from the coast, allowing minimal upwelling on the shelf. Due to the strong advection of warm waters in the surface current, upwelling on the shelf is warmer than initial conditions though relatively cooler than the surface current. As a result, upwelling incurs a weak increase in sound speed and affects a relatively small area.

C. NCCS AND LCS COMPARISON

The objective of this study was to assess which dynamics of EBCs have the greatest impact on the sound speed structure. The NCCS and LCS were chosen for their

unique characteristics, i.e., the Mediterranean Outflow in the Gulf of Cadiz and the anomalous, poleward surface flow off the coast of Australia. As shown in Tables 3 and 4, these characteristics produce a variety of features and results.

The greatest change in sound speed in either region was caused by upwelling in the NCCS. Although the NCCS and the LCS are both influenced by equatorward, upwelling-favorable winds typical of EBC regions, the resultant upwelling differs dramatically between the two systems. In the NCCS, upwelling is present at all latitudes, has an extension on the order of 100 km, and causes a predictable decrease in sound speed due to cold waters. Contrary to this intuitive sound speed decrease in NCCS upwelling, the confined regions of upwelling in the LCS show an increase in sound speed due to the proximity of the surface current. The Leeuwin Current flows along the shelf break, restricting upwelling to the shelf. Consequently, the extent of NCCS upwelling is also significantly larger than the LCS and affects a larger volume of the domain.

Despite differences in upwelling, both the NCCS and LCS surface currents generated eddies of great acoustical significance. Both currents experienced large changes in temperature; the NCCS flow contained cool waters from upwelling and the LCS advected warm waters from the thermohaline gradient. Eddies from either system contained cores of the surface current temperature. Although greater changes in sound were found in the NCCS due to the intensity and extent of upwelling, the LCS model simulated more surface eddies than the NCCS. The LCS surface eddies affected a greater surface area and volume, evidence of a stronger system. Eddies in both areas affected more than half the water column, extending to ~1500 m depth.

Although the LCS is a stronger current system, greater changes in sound speed by the undercurrent were found in the NCCS, particularly to the north of the gulf, due to the presence of the Mediterranean Outflow. The NCCS undercurrent is also narrower and deeper than the LCS, affecting a smaller volume but resulting in very large horizontal gradients of sound speed along the shelf slope. Eddies generated by the undercurrents in both regions are small in diameter and effect less than a 5 m/s change on sound speed. Meddies of the NCCS incur more change than undercurrent eddies of the LCS due to the added salinity of the MO advected by the NCCS undercurrent.

THIS PAGE INTENTIONALLY LEFT BLANK

IV. SUMMARY

The objective of this process-oriented study was to build on previous studies and determine the effects of eastern boundary current (EBC) dynamics on sound speed structure. The Princeton Ocean Model, a bottom-following sigma coordinate model, was used to explore the classical and unique features of two EBCs, the North Canary Current system (NCCS) and the Leeuwin Current system (LCS). The NCCS model simulated the upwelling, equatorward surface current and poleward undercurrent found in classic EBCs, as well as surface and undercurrent eddies and Mediterranean eddies (Meddies). The LCS model simulated the anomalous poleward surface current and equatorward undercurrent that is unique to the region, and the generation of energetic eddies. Using the equation by Chen and Millero (1977), sound speed was calculated for each model run.

In the NCCS, upwelling appeared by day 20 and grew to a maximum extent by day 63. The wide and shallow feature decreased sound speed by ~ 19 m/s on the shelf at all latitudes from the surface to a maximum depth of 500 m. A single surface eddy formed in the south from an upwelling filament, creating a well-defined, cold-core feature of decreasing sound speed. A warm, poleward undercurrent formed and reached maximum intensity without eddies by day 36. The undercurrent increased sound by 5 m/s in the gulf and south, and 9 m/s north of Cabo Roca. After day 36, the undercurrent generated two eddies. The eddy south of the gulf had a weak effect on sound, while the eddy in the north affected south three times more than in the south. These differences in sound speed in the north and south may be attributed to the presence of the Mediterranean Outflow. Water, salty waters of the Mediterranean Outflow are advected northwards in the undercurrent, causing stronger fluctuations in sound speed.

In the LCS model, forcing from the thermal gradient overwhelmed wind stress, causing the strong, narrow Leeuwin Current to form by day 20. The current reached maximum intensity without eddies by day 36. Unlike classical EBCs, warm water was advected poleward within the flow, incurring a ~ 12 m/s increase in sound speed. An equatorward undercurrent formed simultaneously, narrowing considerably from south to north and advecting cold water from the polar region. The undercurrent had a smaller

effect on sound speed than the surface current and caused a decrease in sound. Southerly winds generated upwelling on the shelf in regions where the surface current had deviated from the coast. Although upwelled waters were relatively cooler than the surface current, upwelling caused a weak increase in sound from initial conditions. Energetic eddies formed by day 45 and continued to appear and grow through day 63. Eddies were warm-core on the surface and cold-core in the undercurrent, typically affecting a large volume of the domain and the entire water column. These features increased sound speed from the surface to ~1500 m depth, and then decreased sound speed to ~2500 m depth.

The dynamics of EBCs lead to large changes in sound speed (5-15 m/s) and distort the vertical sound speed profile. The greatest change in sound speed from initial condition in either region was caused by upwelling in the NCCS. Surface and associated subsurface eddies in the LCS were the largest scale feature in the study. The undercurrent of the NCCS and Meddies presented the most intense (horizontal and vertical) gradients of sound speed change, incurring a significant change in sound across a relatively small feature. Although the LCS is a stronger current system, greater changes in sound speed by the undercurrent were found in the NCCS, particularly to the north of the gulf, due to the presence of the Mediterranean Outflow. Recommendations for further research include systematically investigating of the effects of each forcing mechanism on sound speed. Longer model runs would allow statistical analysis of individual features, determining the space and temporal correlation of upwelling, eddies, filaments, etc. Acoustic fields and ray traces may be computed with additional vertical layers in the model.

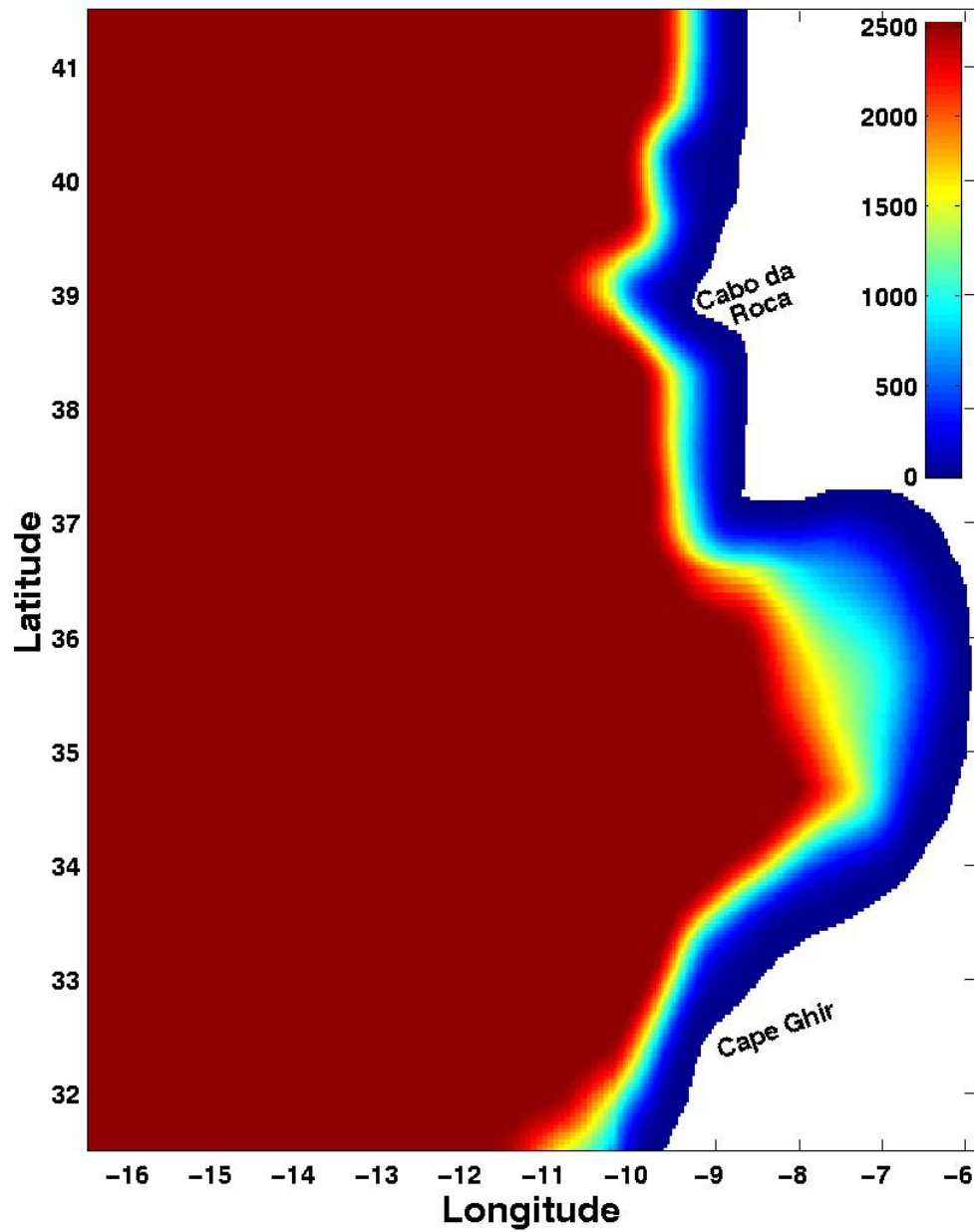


Figure 1. NCCS smoothed topography with depth in meters after applying a linear two-dimensional low-pass filter. (From: Sandwell and Smith (1996))

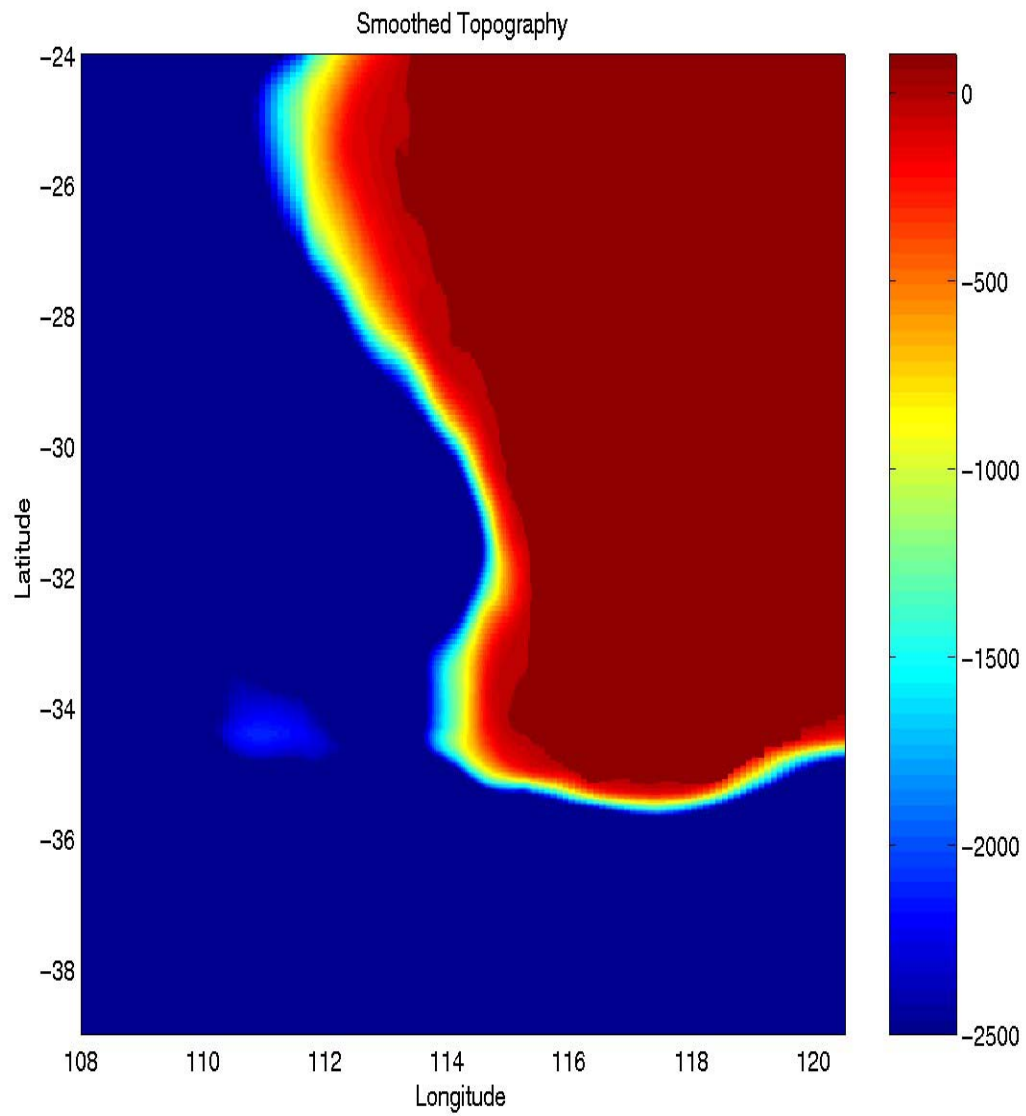


Figure 2. LCS smoothed topography with depth in meters after applying a one-dimensional, iterative filter. Depth is in meters.

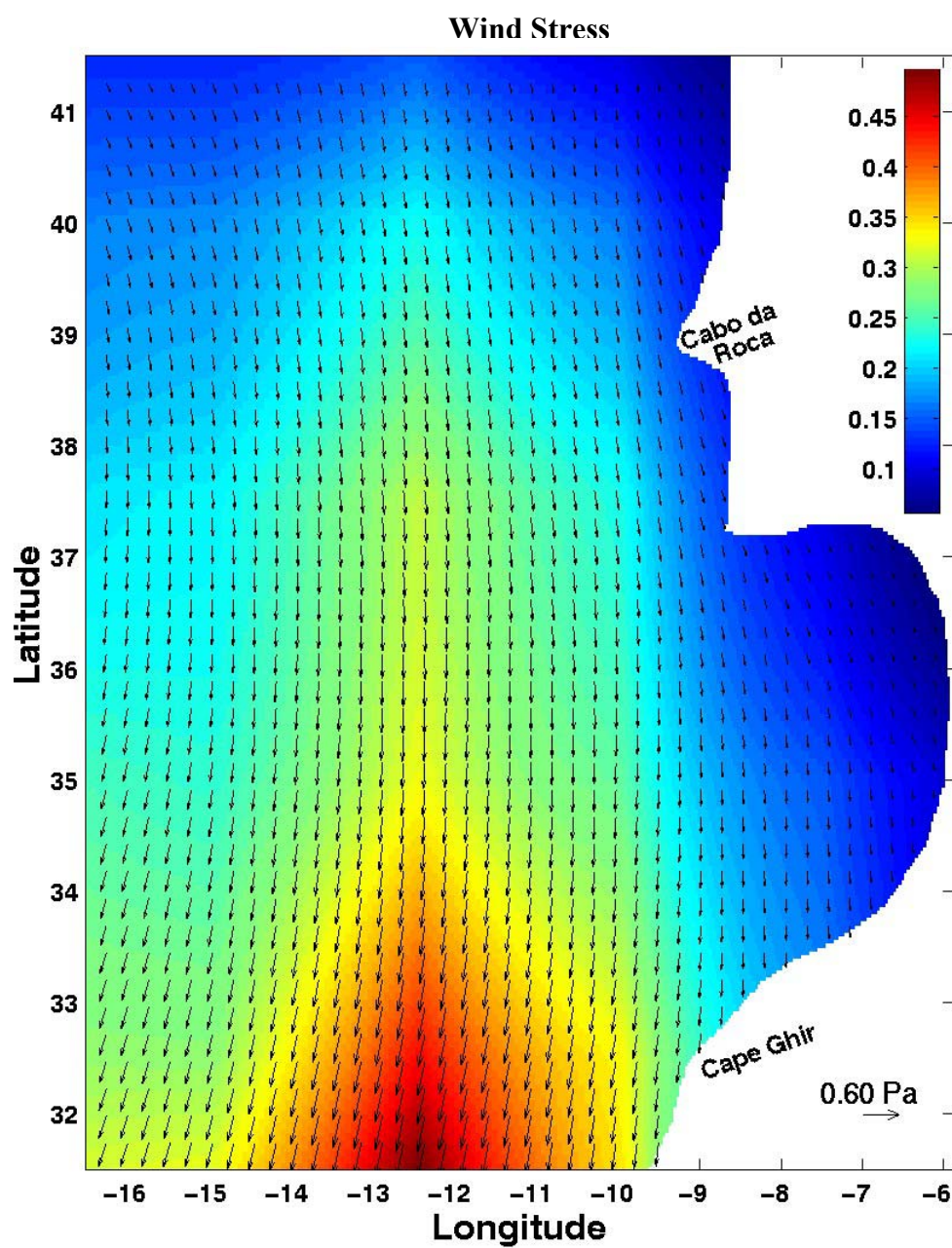


Figure 3. NCCS wind stress vector and magnitude (in color) in Pascals calculated from annual climatological ECMWF winds (From: Trenberth et al., 1990)

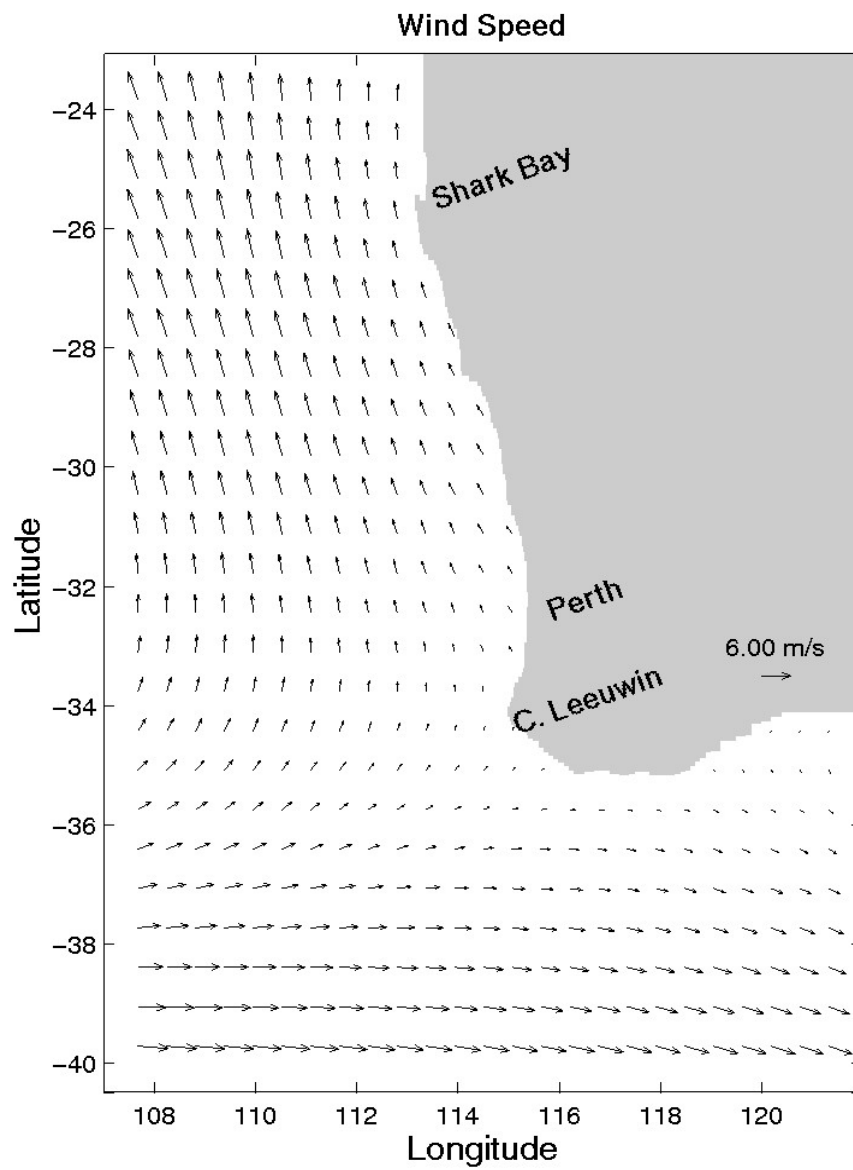


Figure 4. LCS annual average wind in m/s from climatological ECMWF winds obtained (From: Trenberth et al., 1990)

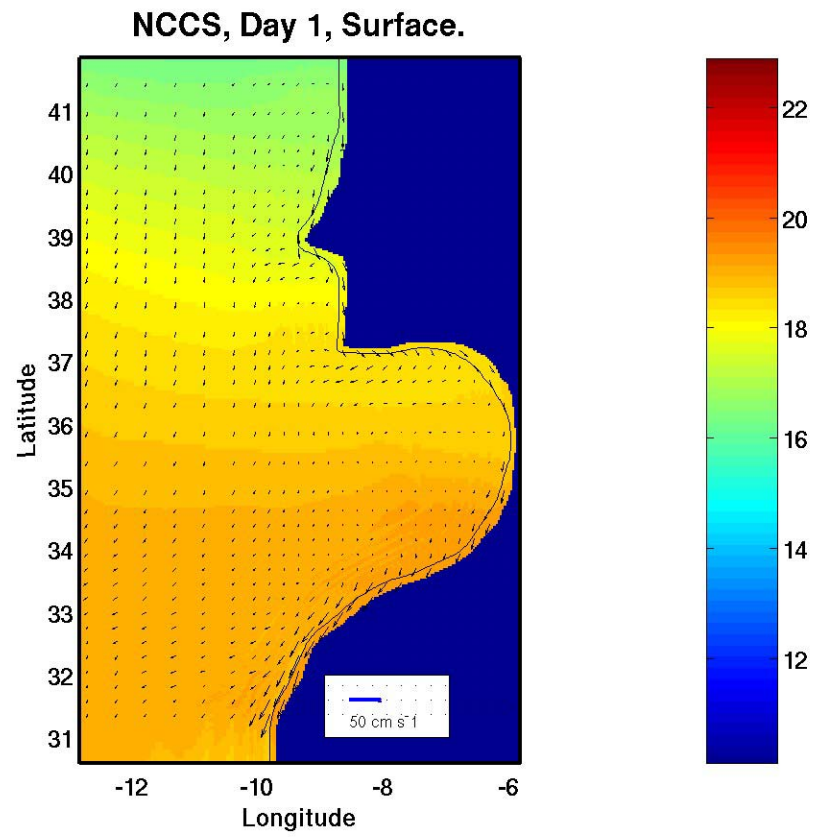


Figure 5. NCCS, Surface temperature ($^{\circ}\text{C}$) and velocity vectors (cm/s) on day 1.

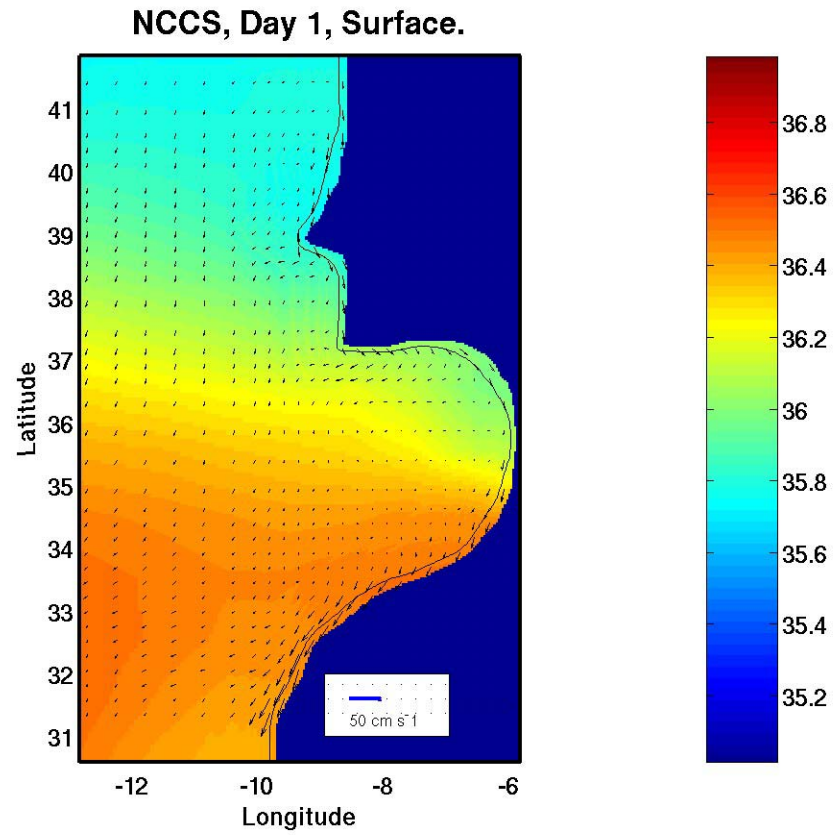


Figure 6. NCCS, Surface salinity (psu) and velocity vectors (cm/s) on day 1.

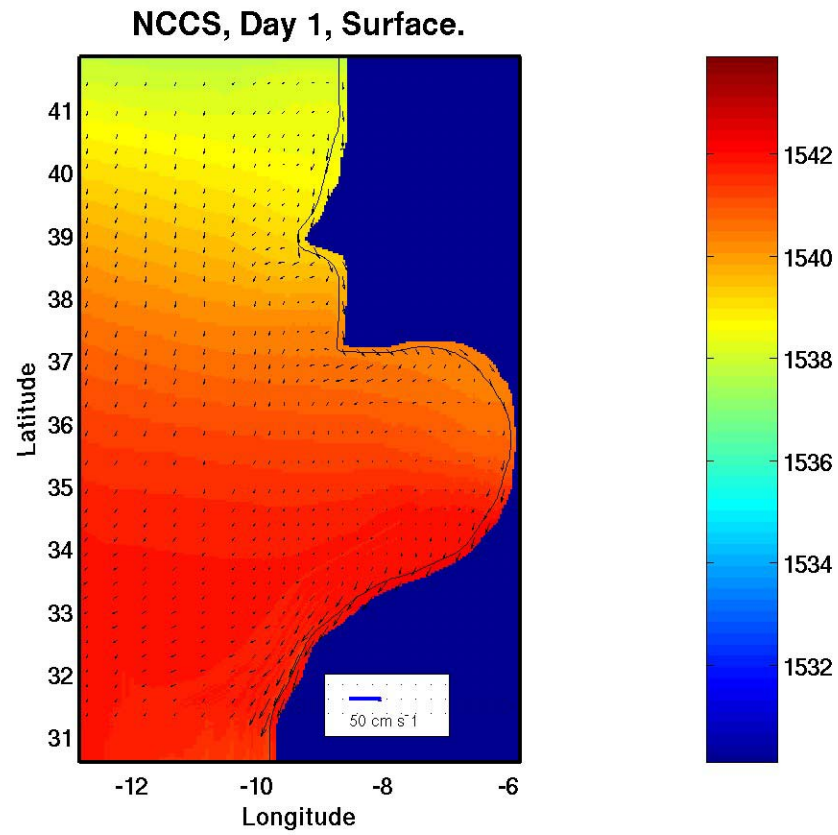


Figure 7. NCCS, Surface sound speed (m/s) and velocity vectors (cm/s) on day 1.

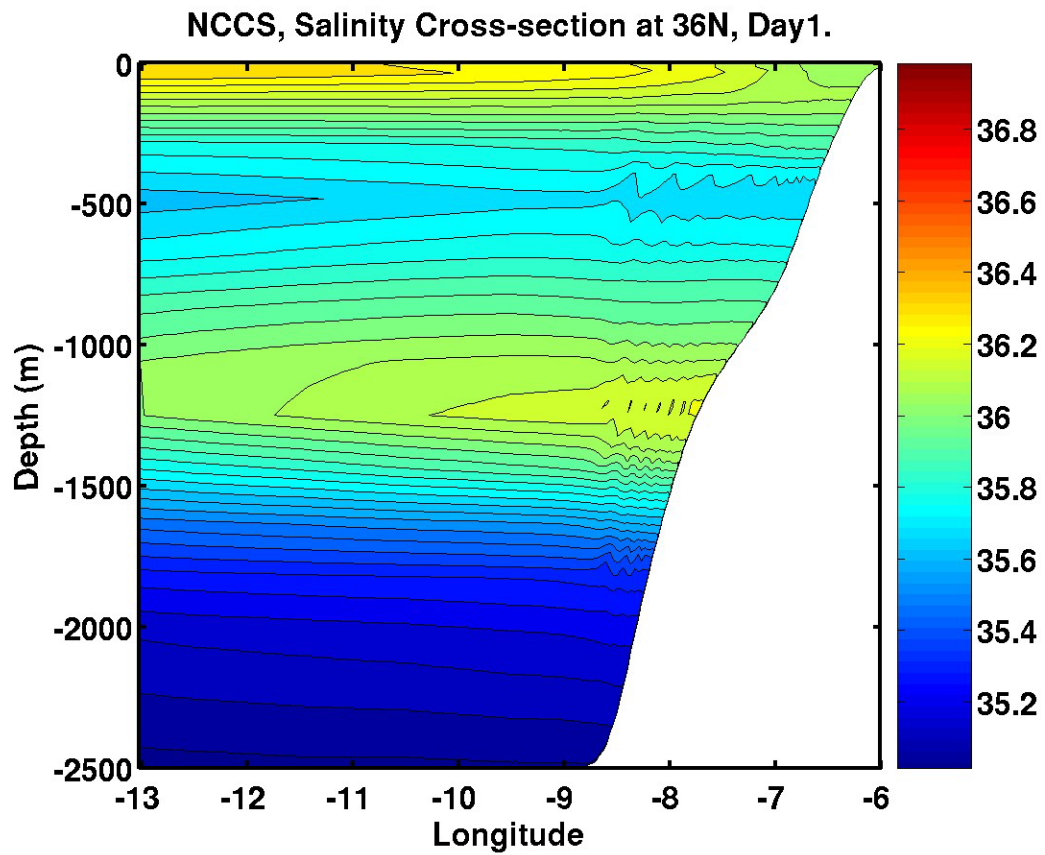


Figure 8. NCCS, Salinity (psu) cross-section at 36°N on day 1.

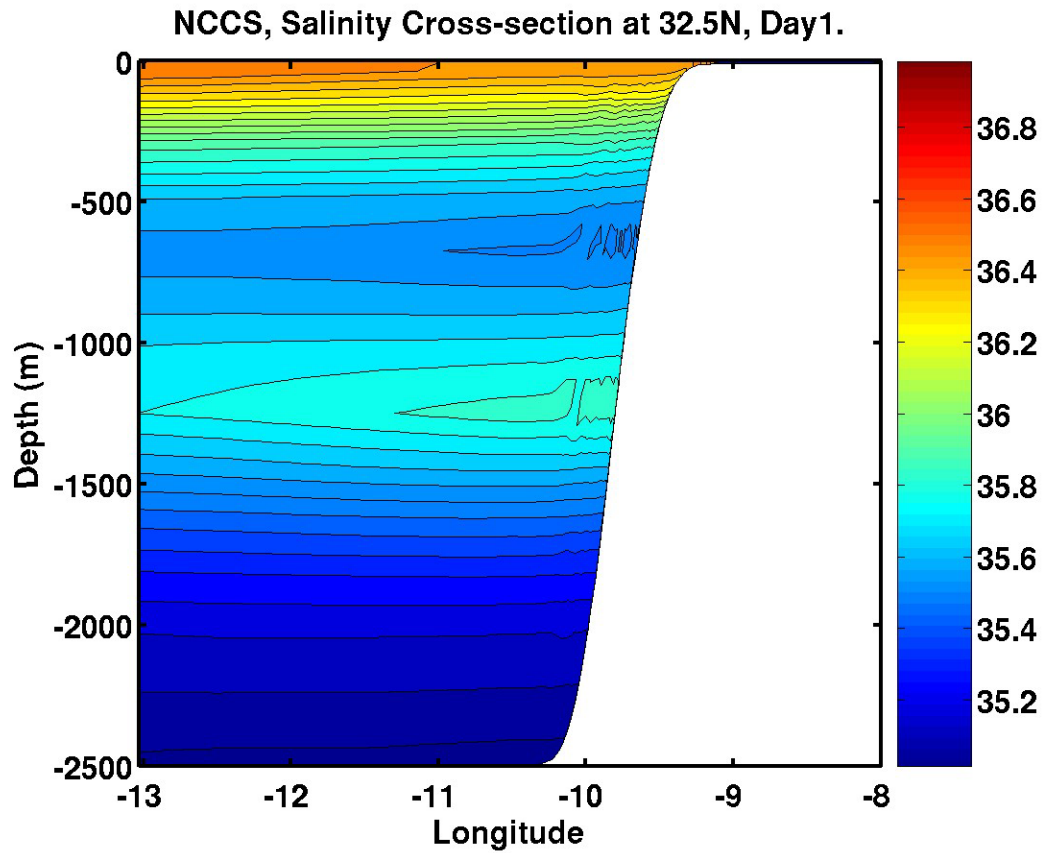


Figure 9. NCCS, Salinity (psu) cross-section at 32.5°N on day 1.

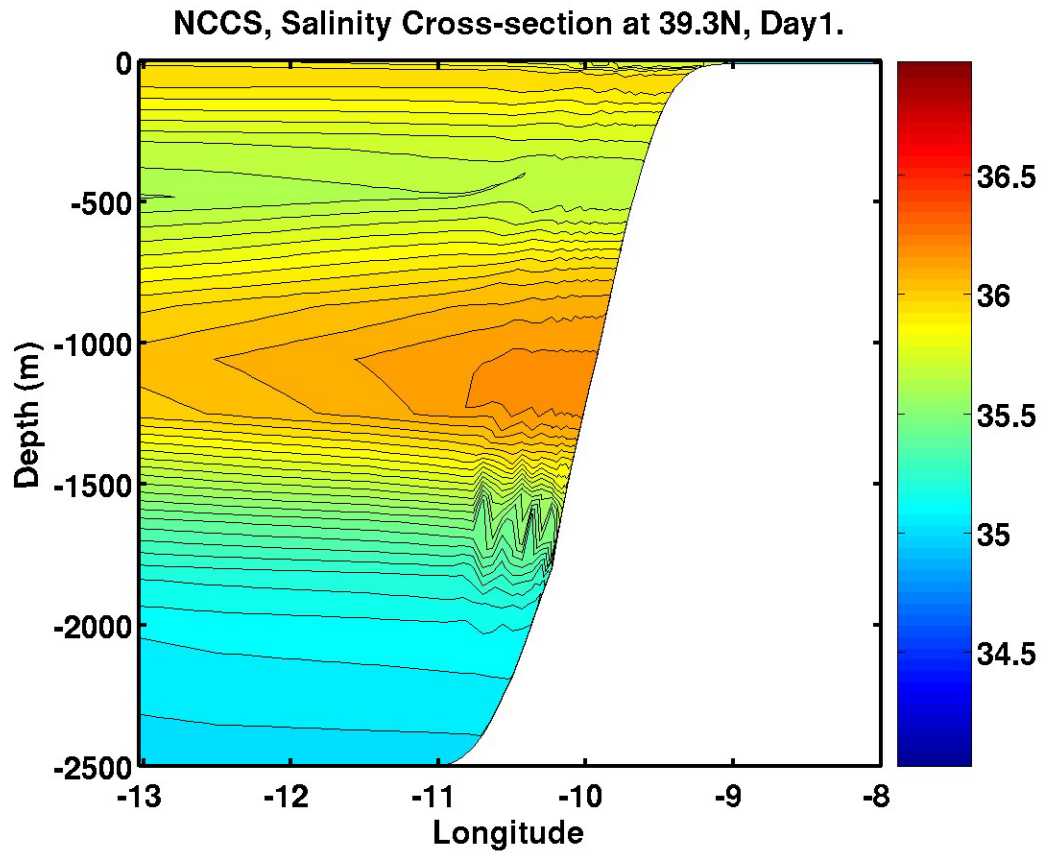


Figure 10. NCCS, Salinity (psu) cross-section at 39.3°N on day 1.

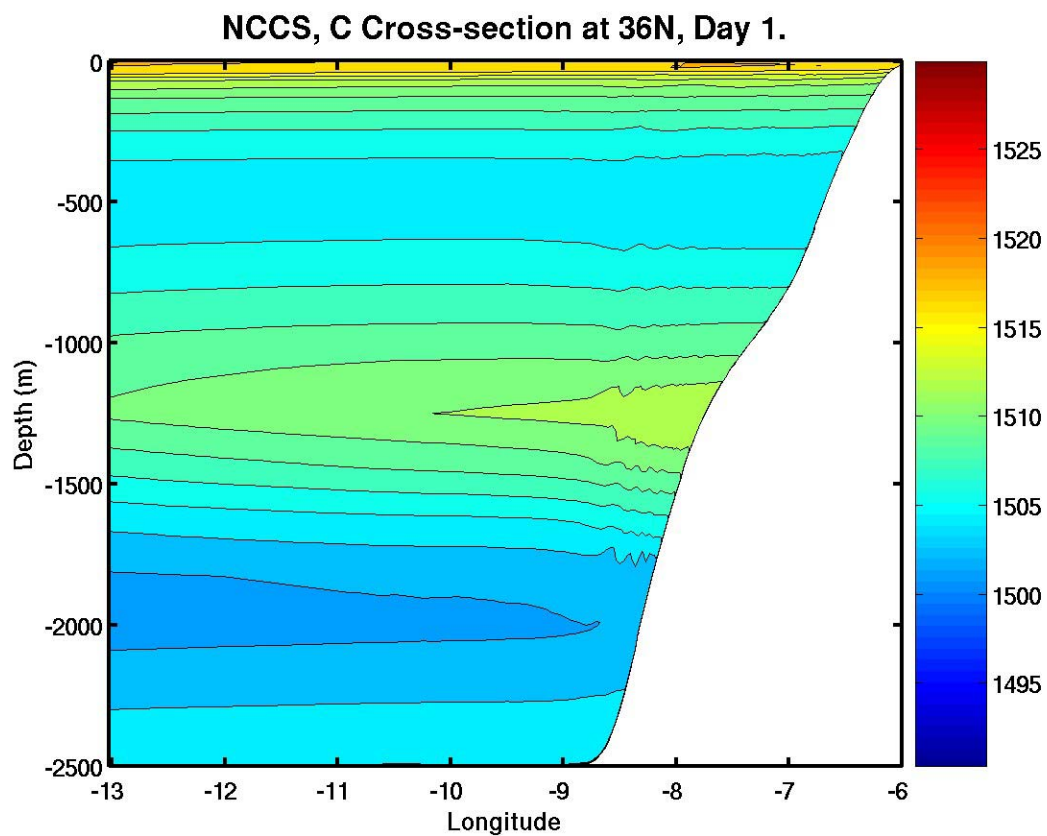


Figure 11. NCCS, Sound speed (m/s) cross-section at 36°N on day 1.

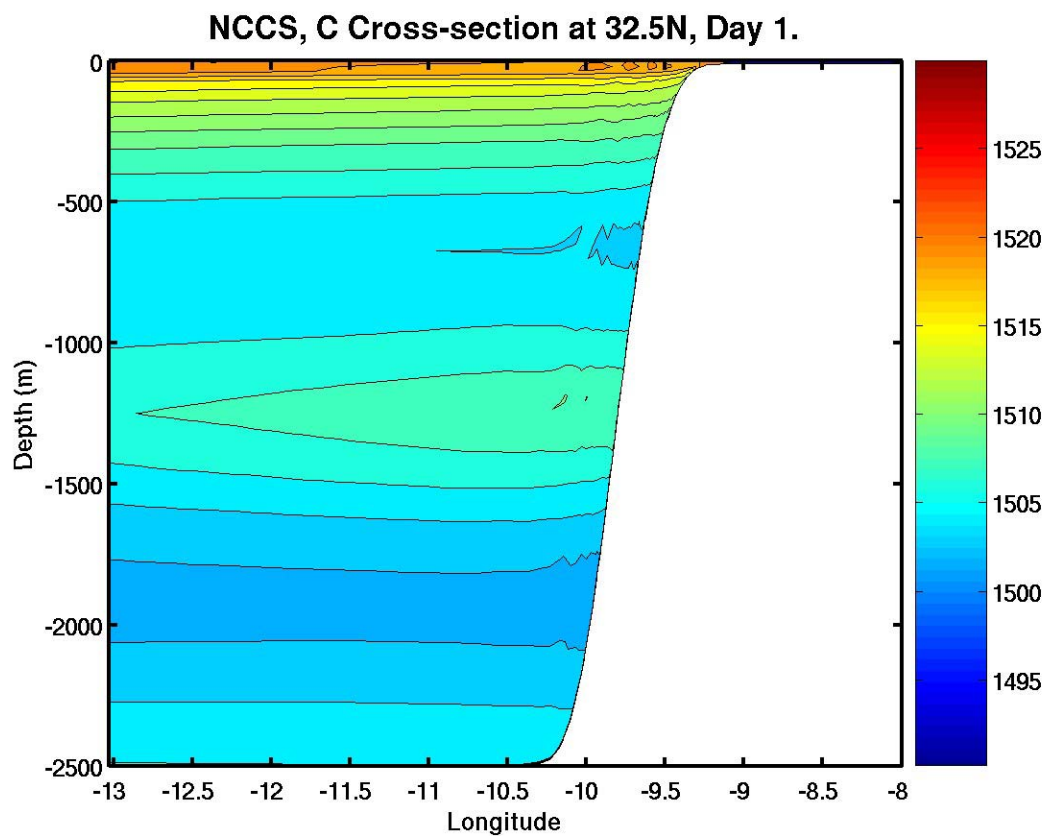


Figure 12. NCCS, Sound speed (m/s) cross-section 32.5°N on day 1.

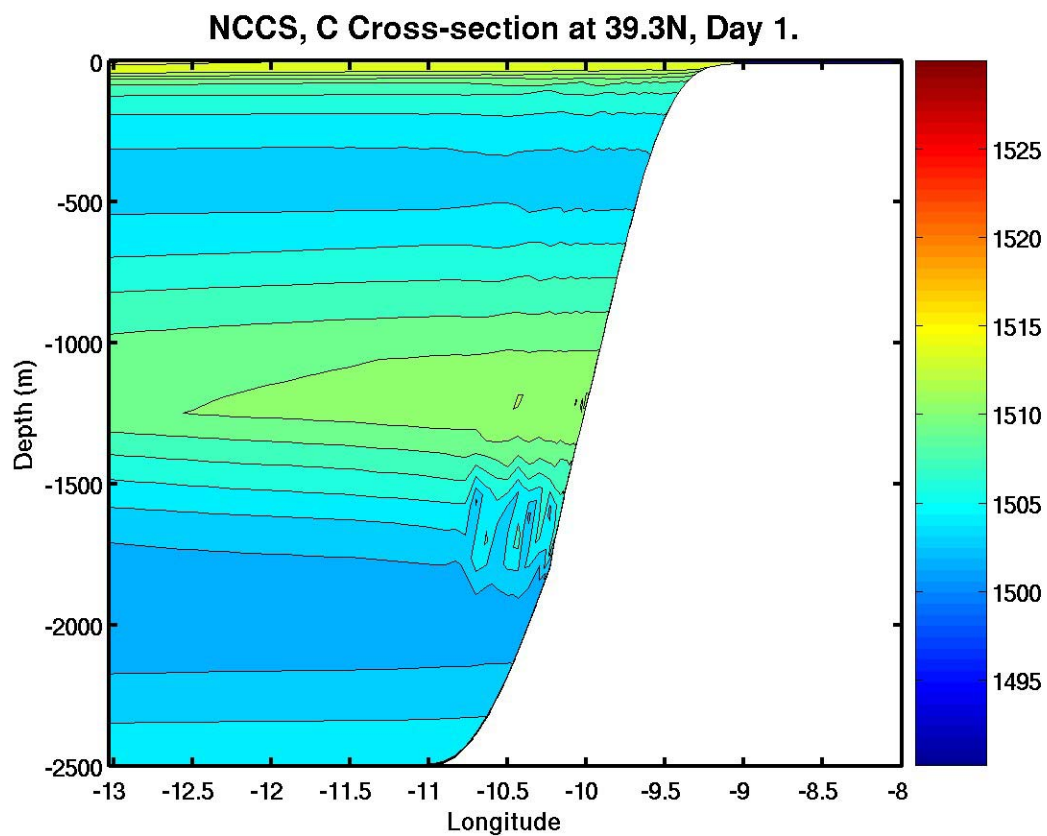


Figure 13. NCCS, Sound speed (m/s) cross-section 39.3°N on day 1.

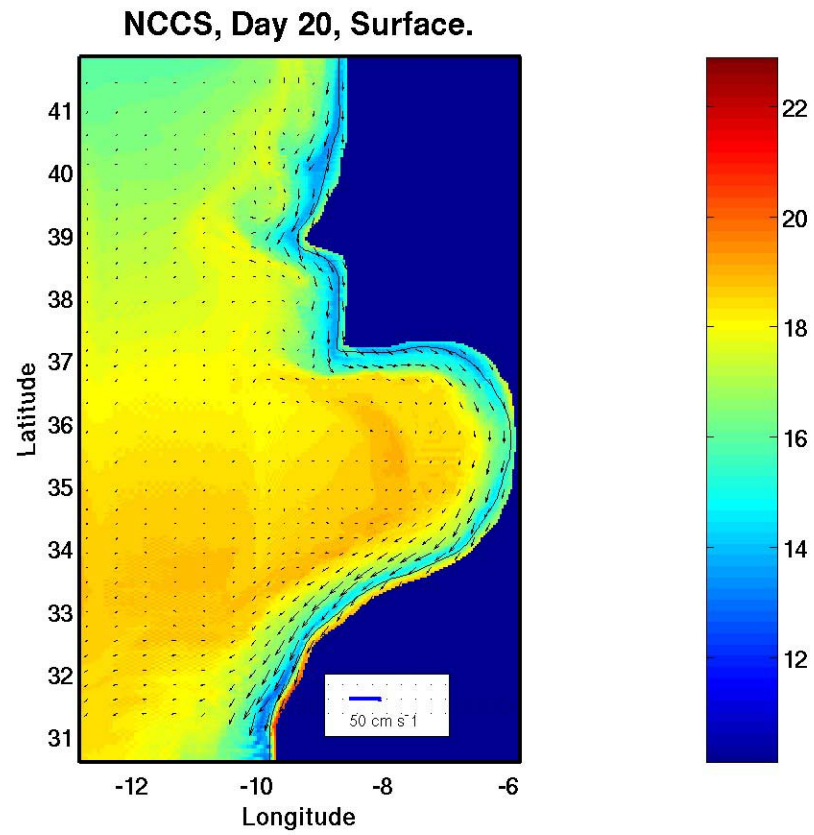


Figure 14. NCCS, Surface temperature (°C) and velocity vectors (cm/s) on day 20.

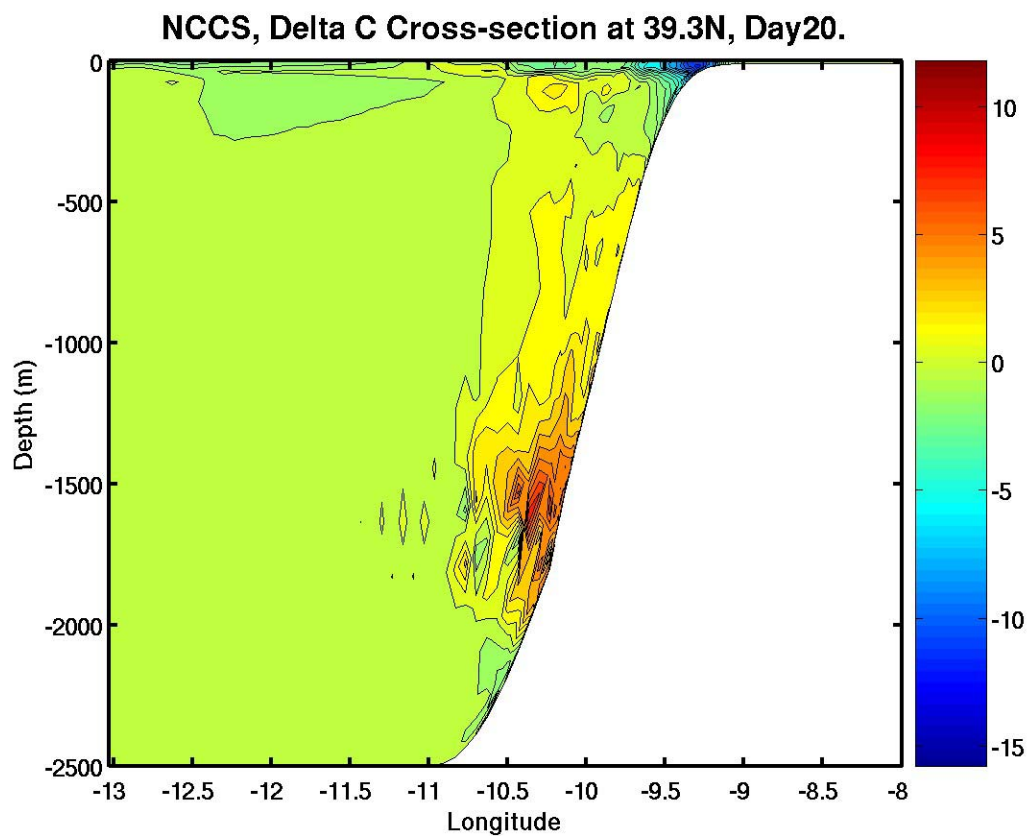


Figure 15. NCCS, Difference in sound speed (m/s) from initial conditions, cross-section at 39.3°N on day 20.

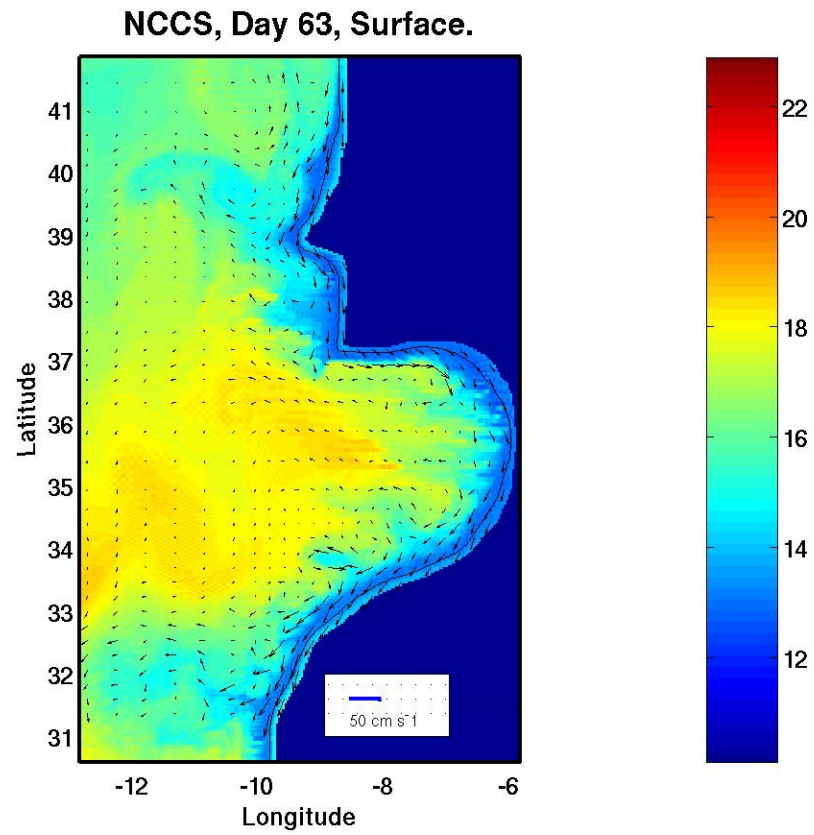


Figure 16. NCCS, Surface temperature (°C) and velocity vectors (cm/s) on day 63.

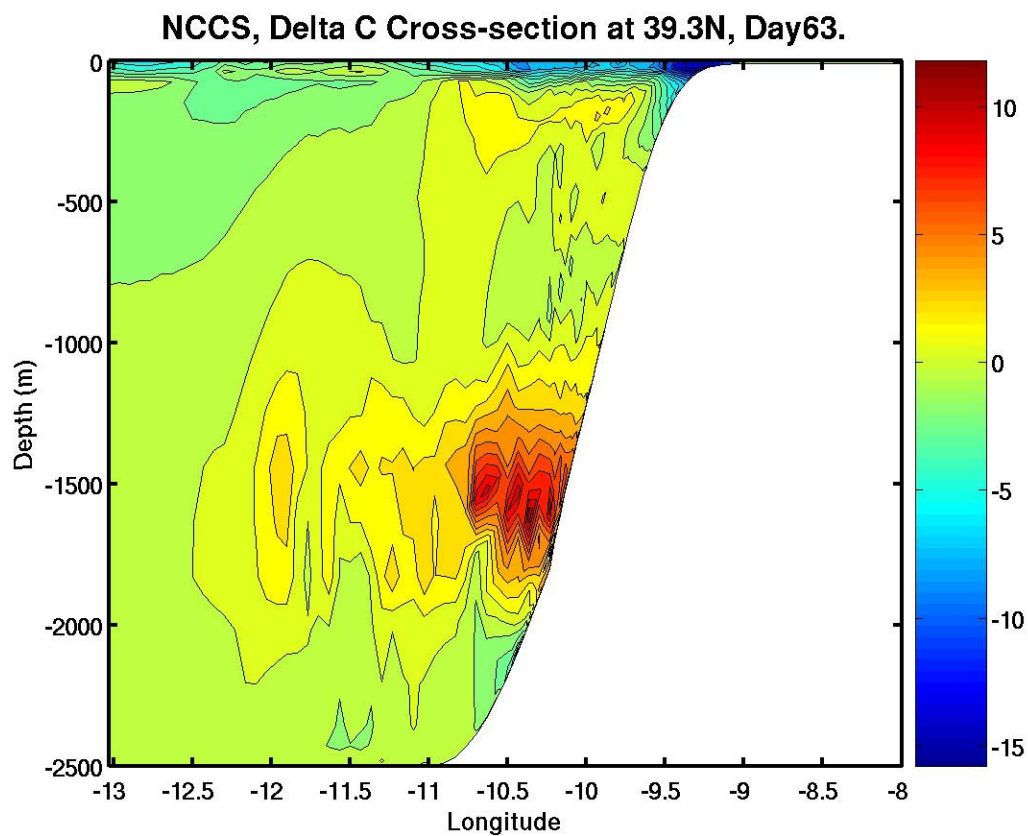


Figure 17. NCCS, Difference in sound speed (m/s) from initial conditions, cross-section at 39.3°N on day 63.

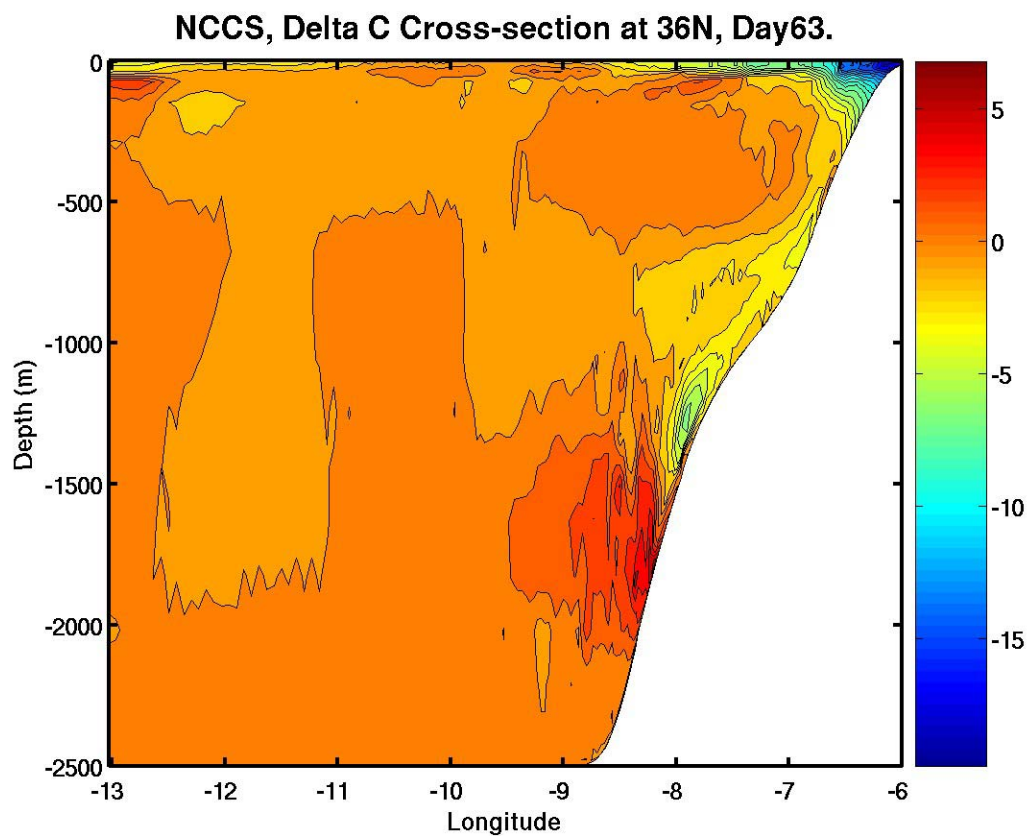


Figure 18. NCCS, Difference in sound speed (m/s) from initial conditions, cross-section at 36°N on day 63.

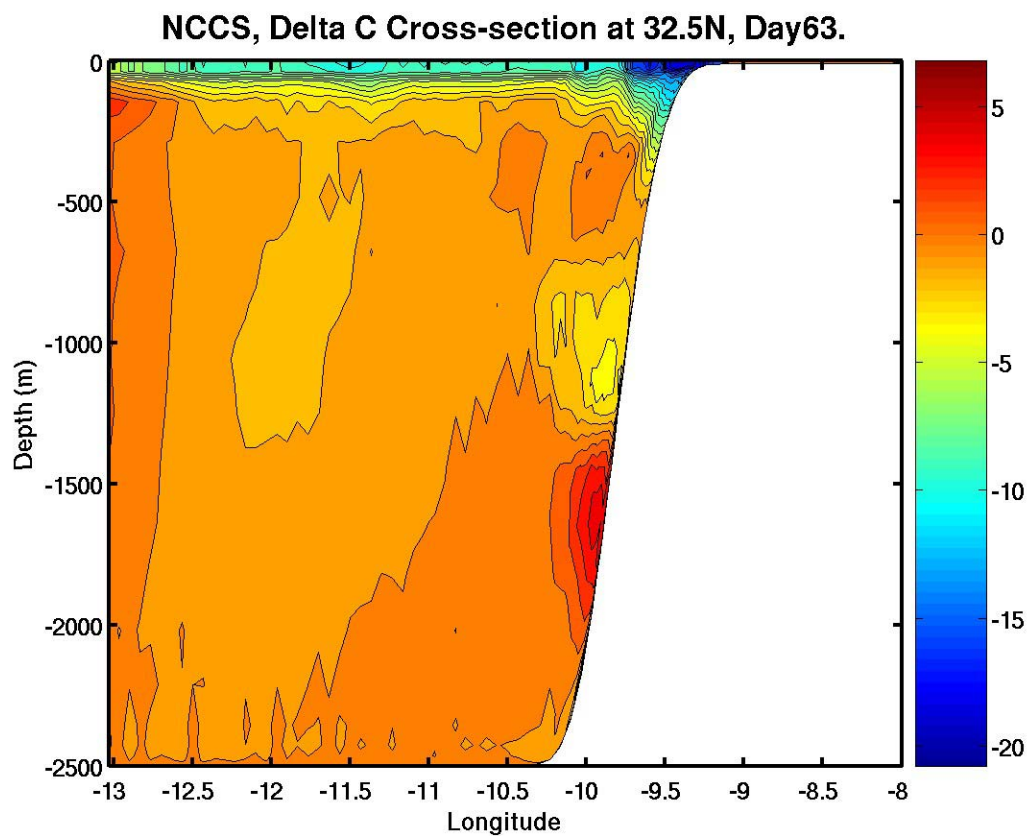


Figure 19. NCCS, Difference in sound speed (m/s) from initial conditions, cross-section at 32.5°N on day 63.

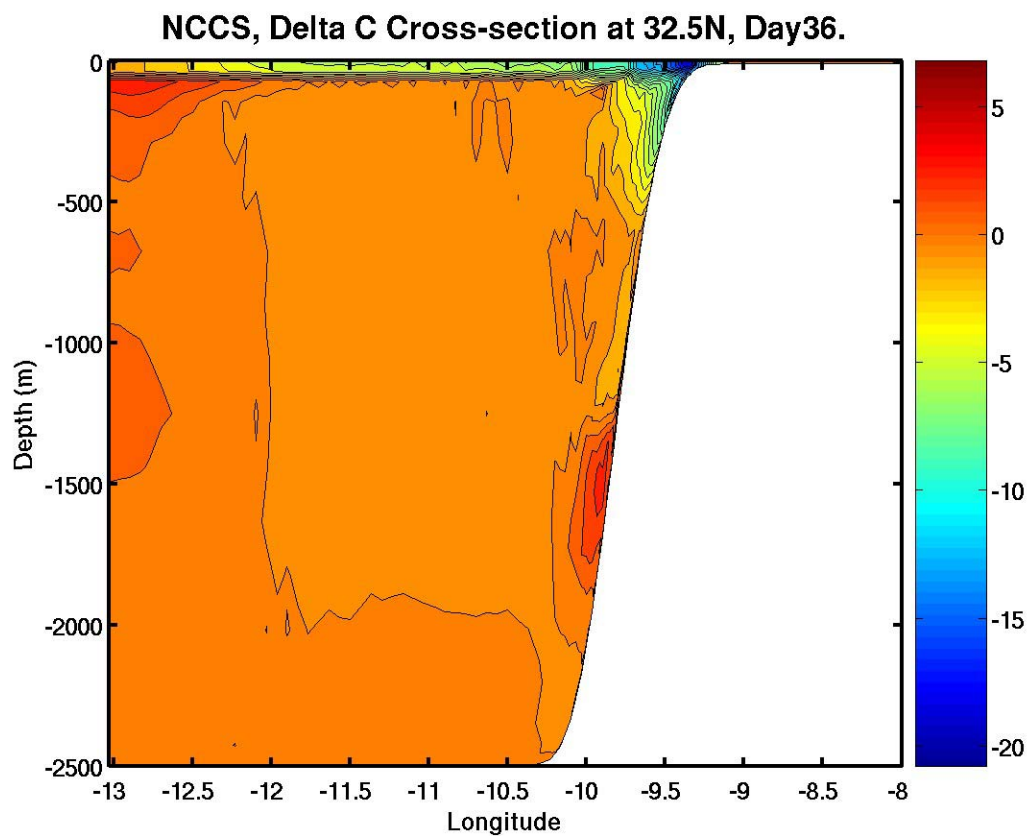


Figure 20. NCCS, Difference in sound speed (m/s) from initial conditions, cross-section at 32.5°N on day 36.

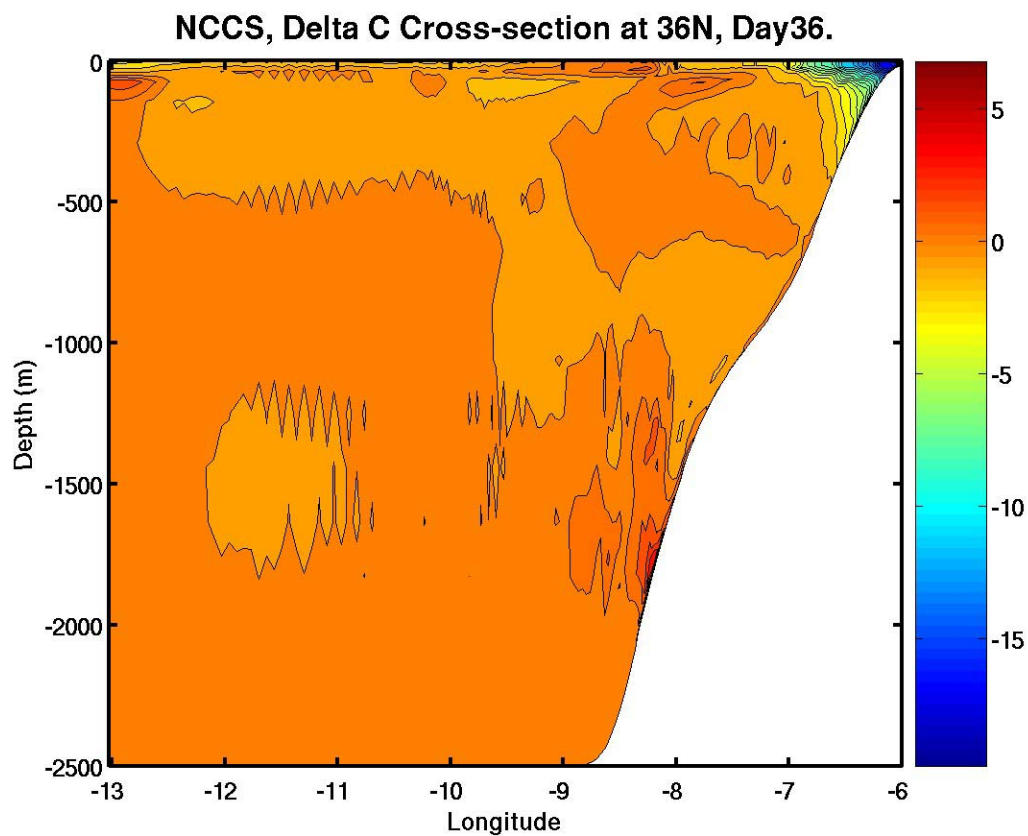


Figure 21. NCCS, Difference in sound speed (m/s) from initial conditions, cross-section at 36°N on day 36.

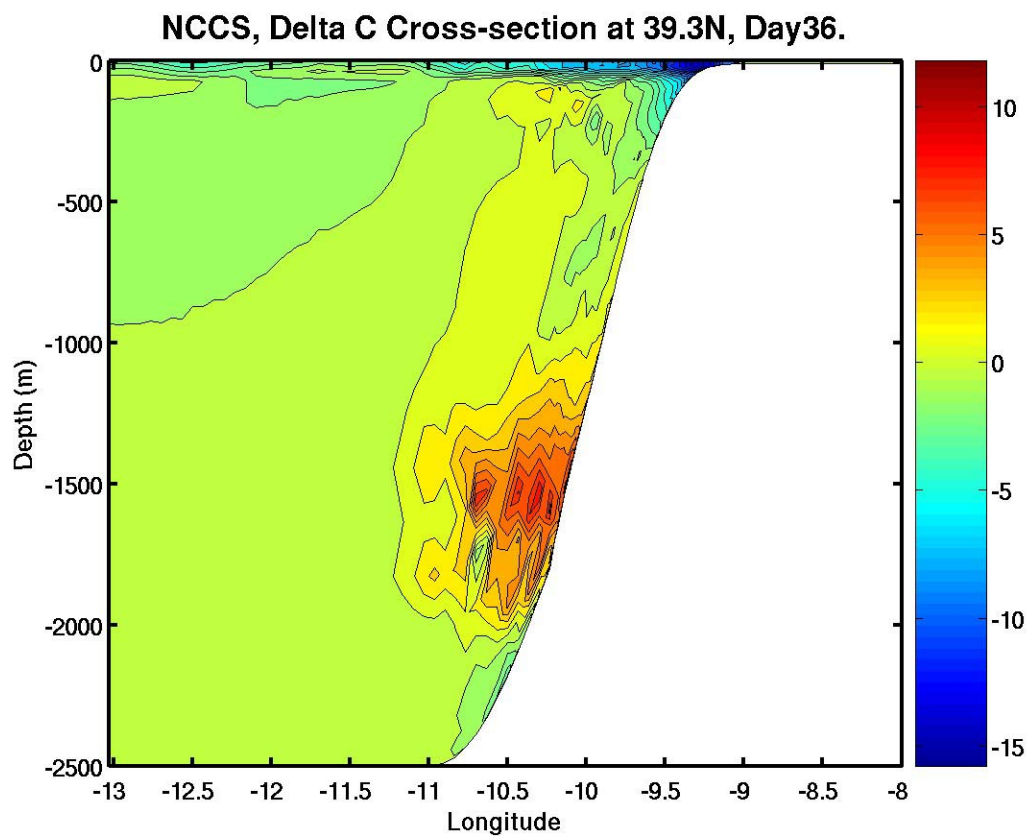


Figure 22. NCCS, Difference in sound speed (m/s) from initial conditions, cross-section at 39.3°N on day 36.

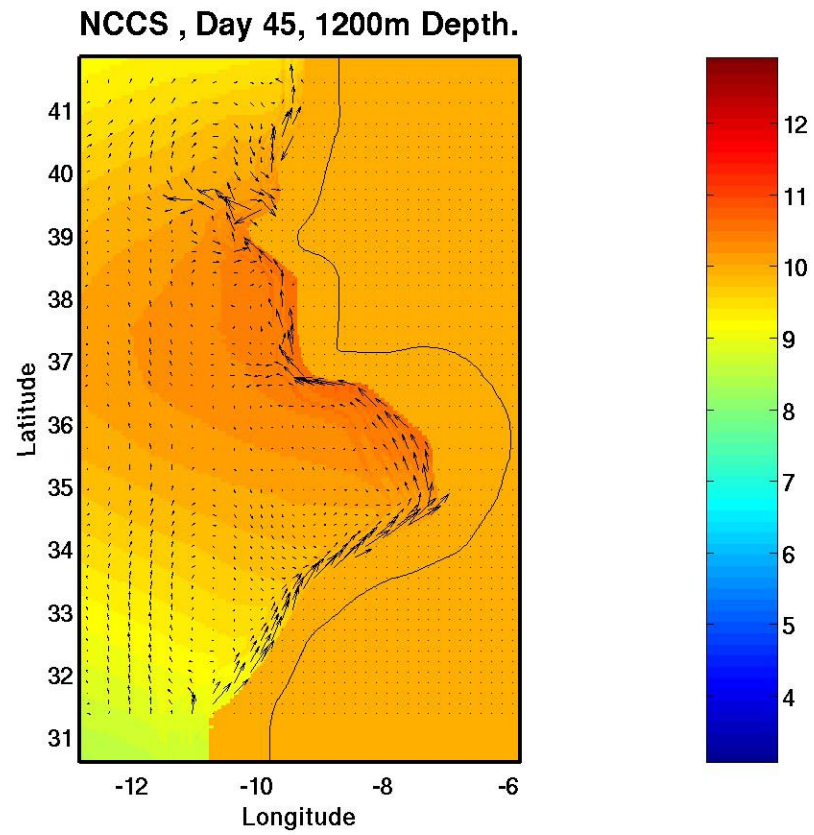


Figure 23. NCCS, Temperature ($^{\circ}\text{C}$) and velocity (cm/s) at 1200 m depth on day 45.

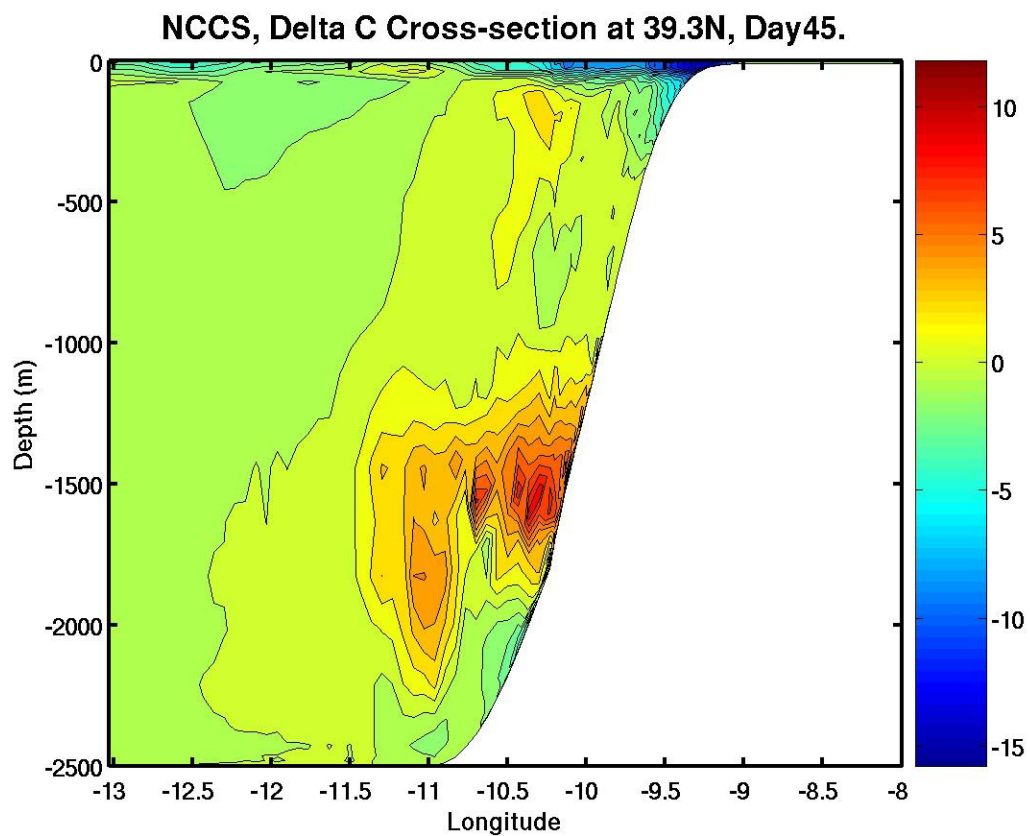


Figure 24. NCCS, Difference in sound speed (m/s) from initial conditions, cross-section at 39.3°N on day 45.

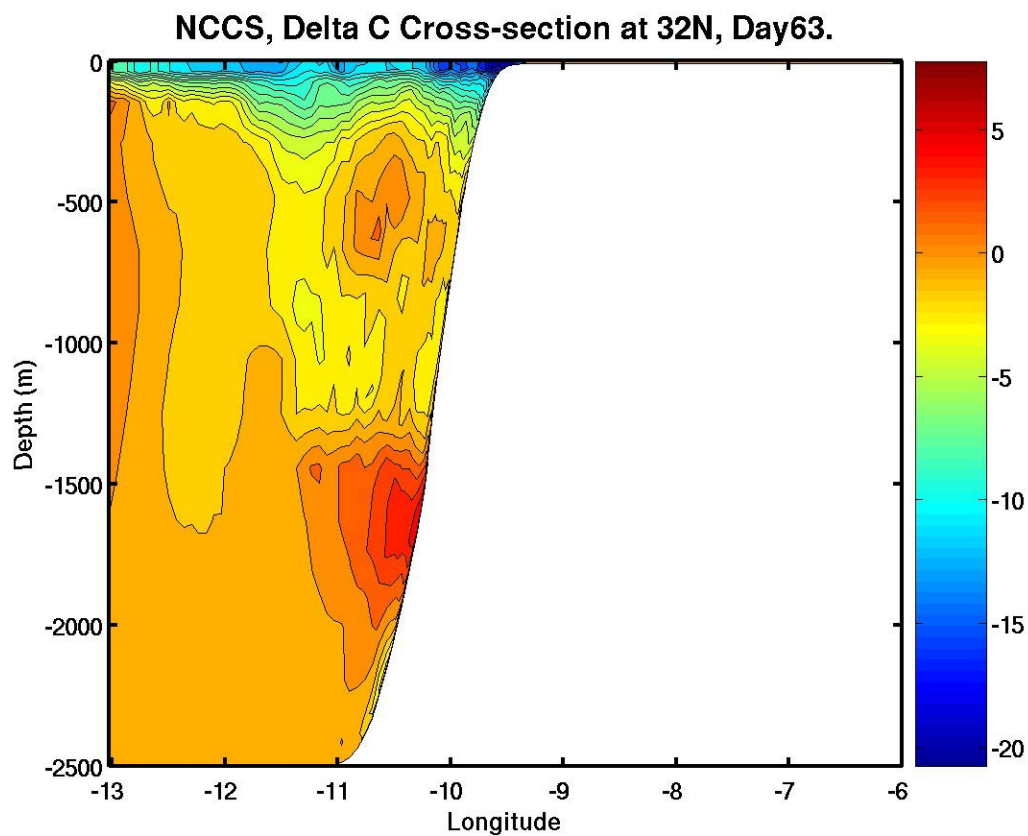


Figure 25. NCCS, Difference in sound speed (m/s) from initial conditions, cross-section at 32°N on day 63.

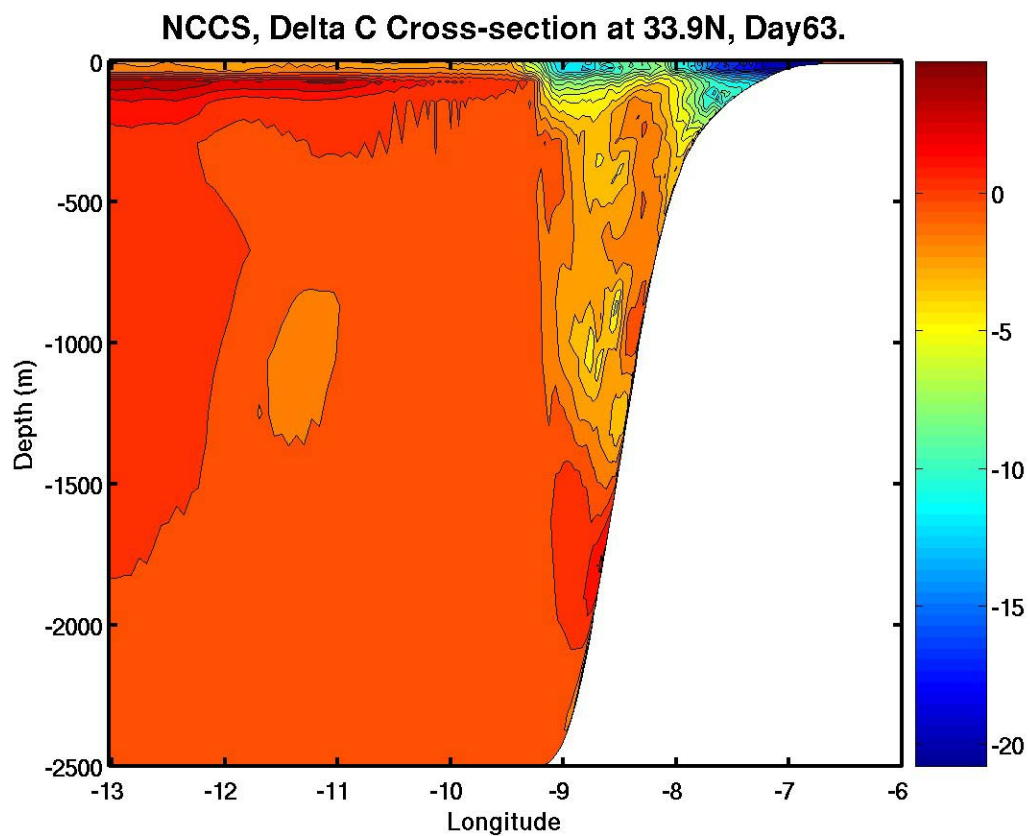


Figure 26. NCCS, Difference in sound speed (m/s) from initial conditions, cross-section at 33.9°N on day 63.

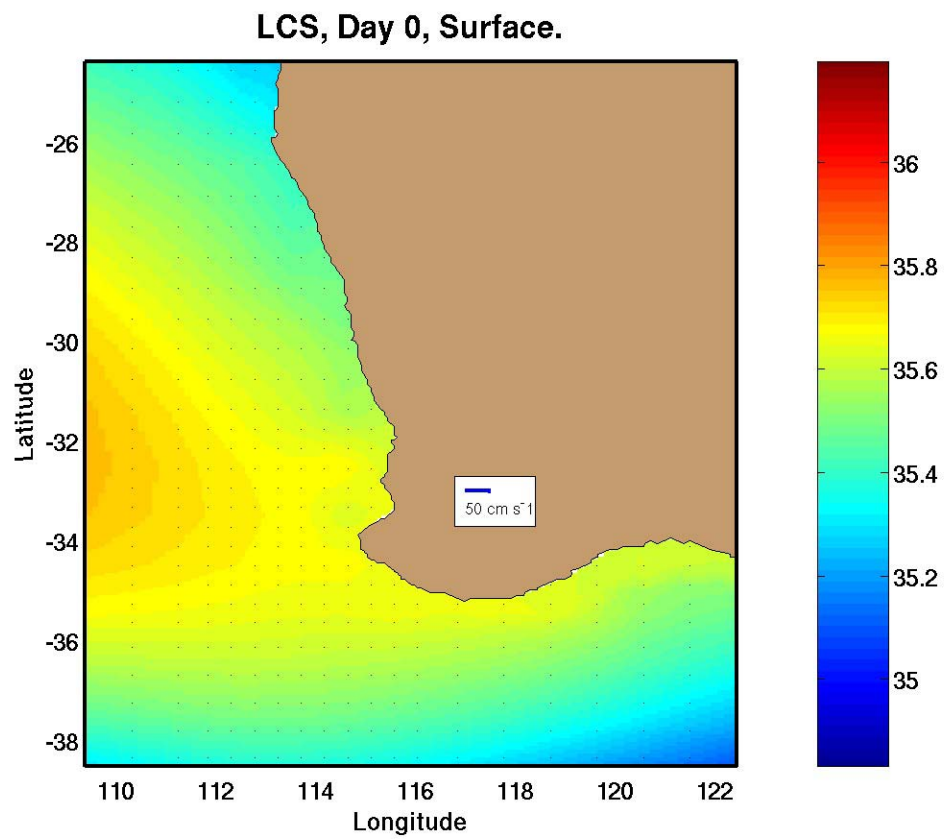


Figure 27. LCS, Initial conditions of surface salinity (psu).

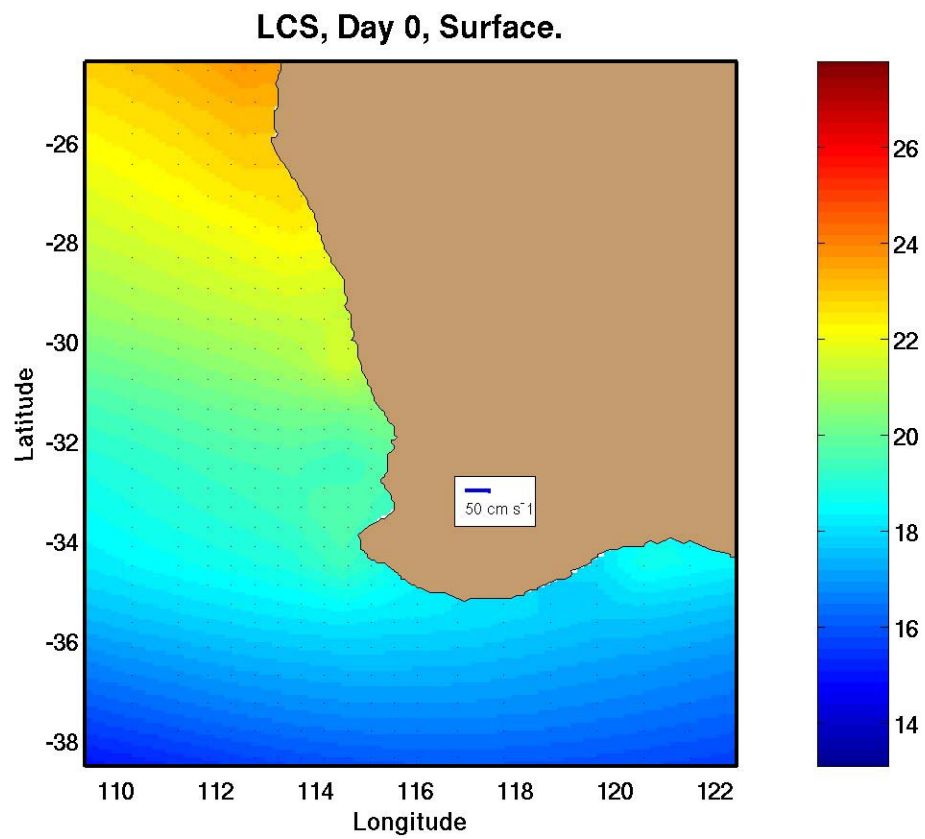


Figure 28. LCS, Initial conditions of surface temperature (°C).

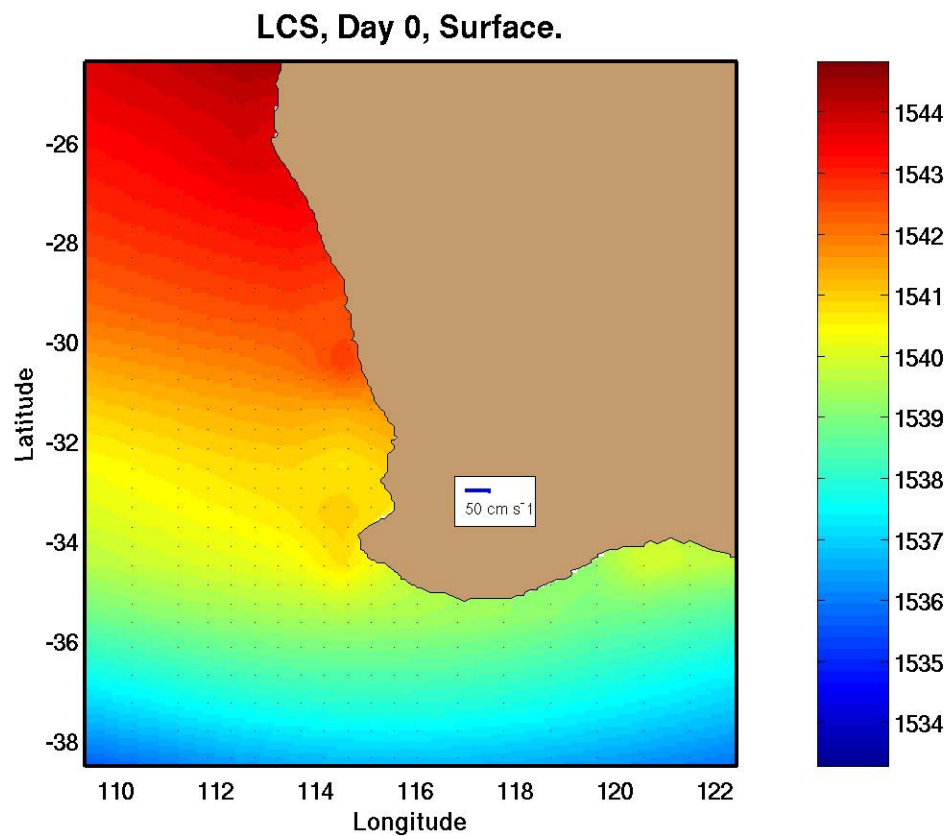


Figure 29. LCS, Initial conditions of surface sound speed (m/s).

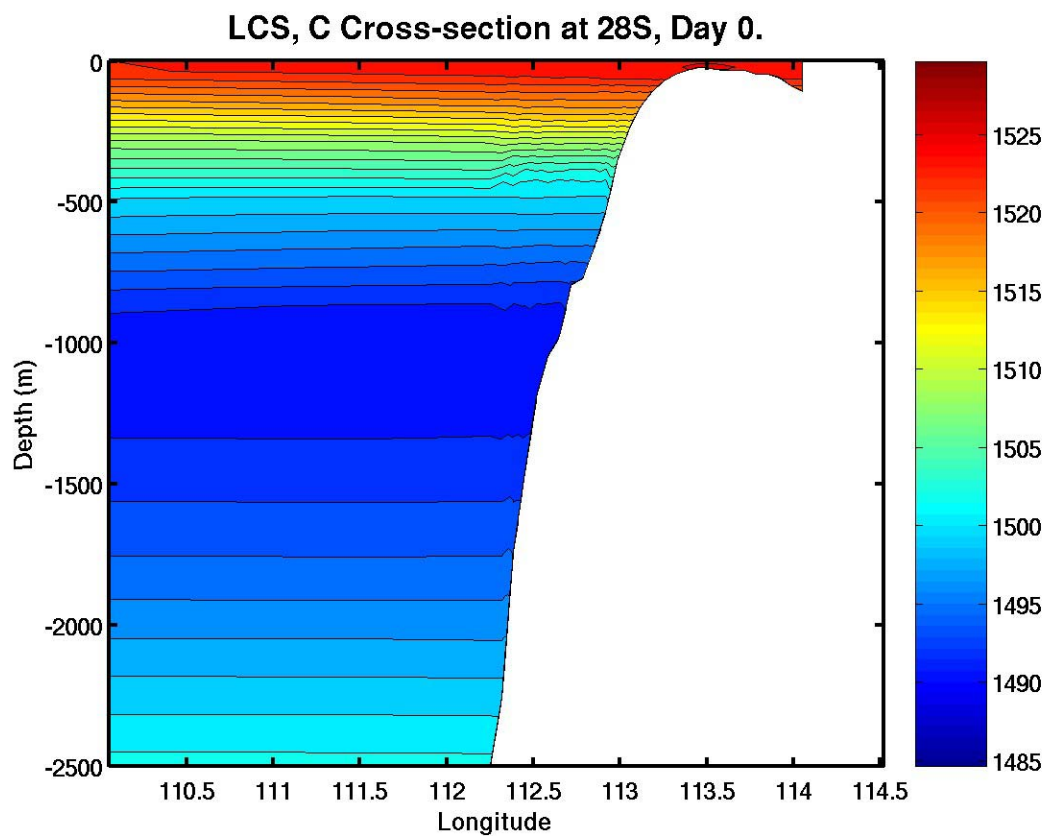


Figure 30. LCS, Sound speed (m/s) cross-section at 28°S for initial conditions.

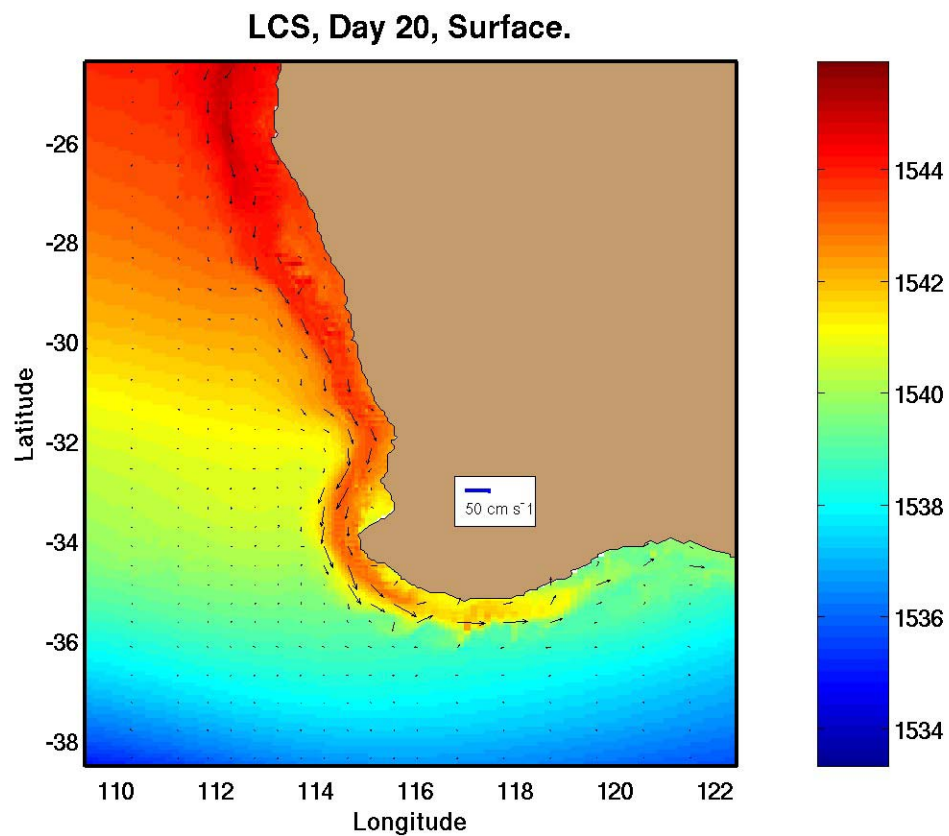


Figure 31. LCS, Surface sound speed (m/s) and velocity vectors (cm/s) on day 20.

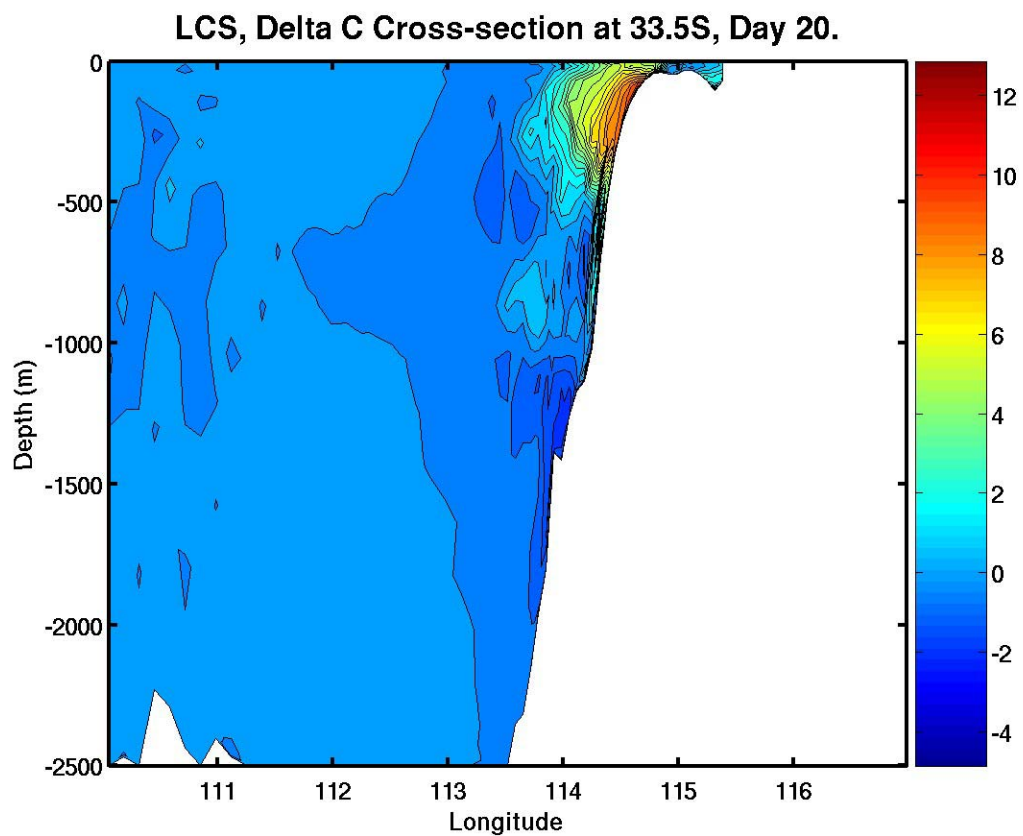


Figure 32. LCS, Difference in sound speed (m/s) from initial conditions, cross-section at 33.5°S on day 20.

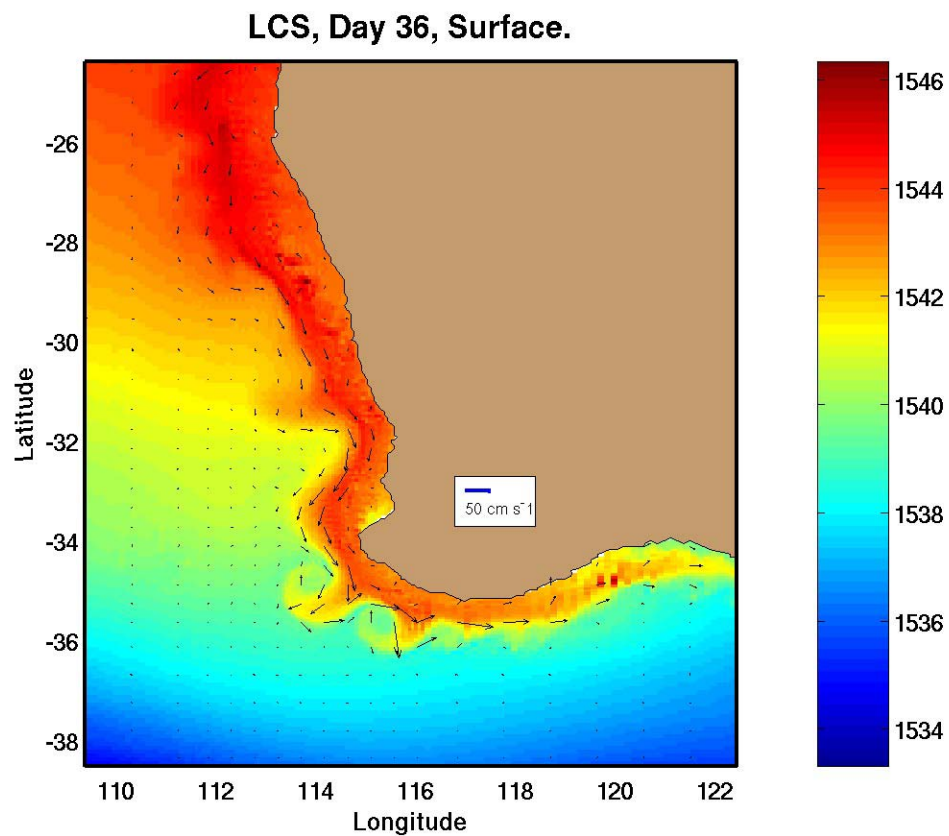


Figure 33. LCS, Surface sound speed (m/s) and velocity vectors (cm/s) on day 36.

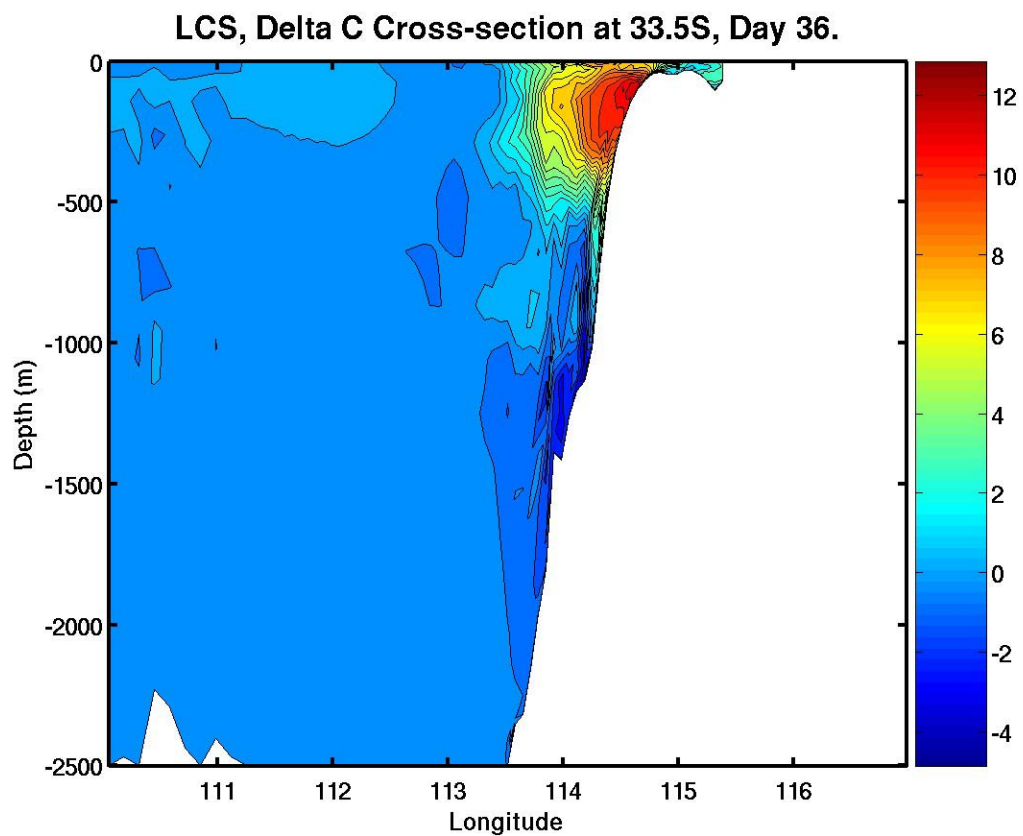


Figure 34. LCS, Difference in sound speed (m/s) from initial conditions, cross-section at 33.5°S on day 36.

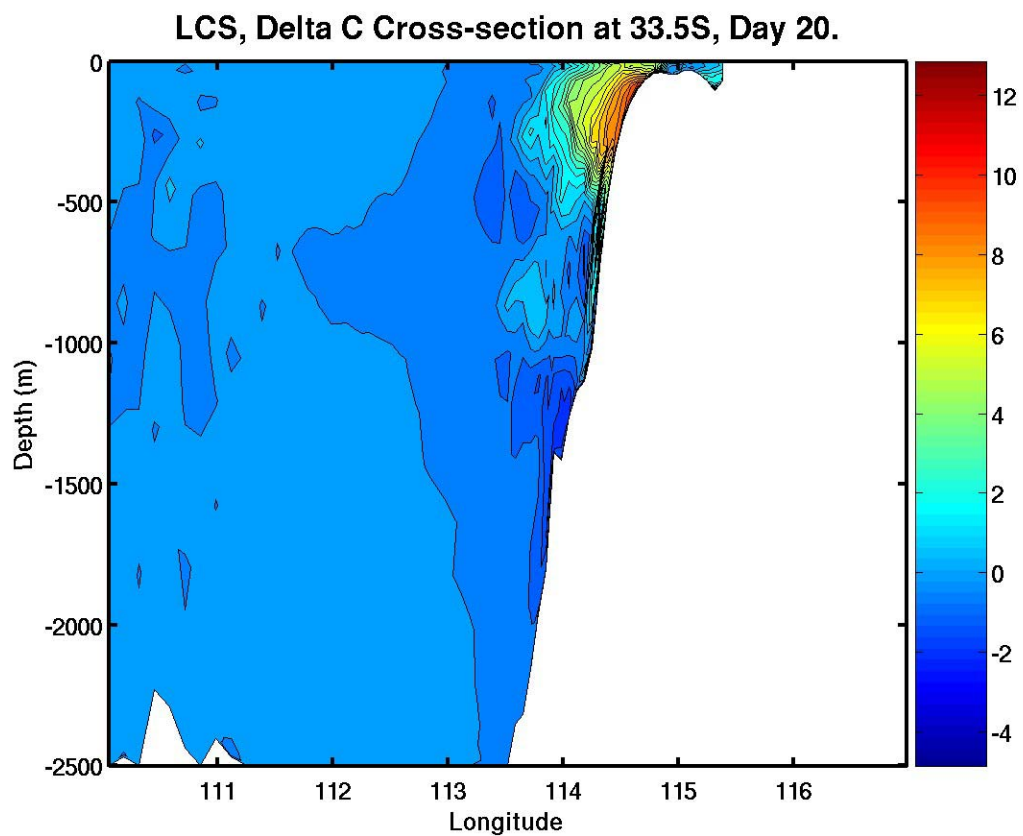


Figure 35. LCS, Difference in sound speed (m/s) from initial conditions, cross-section at 33.5°S on day 20.

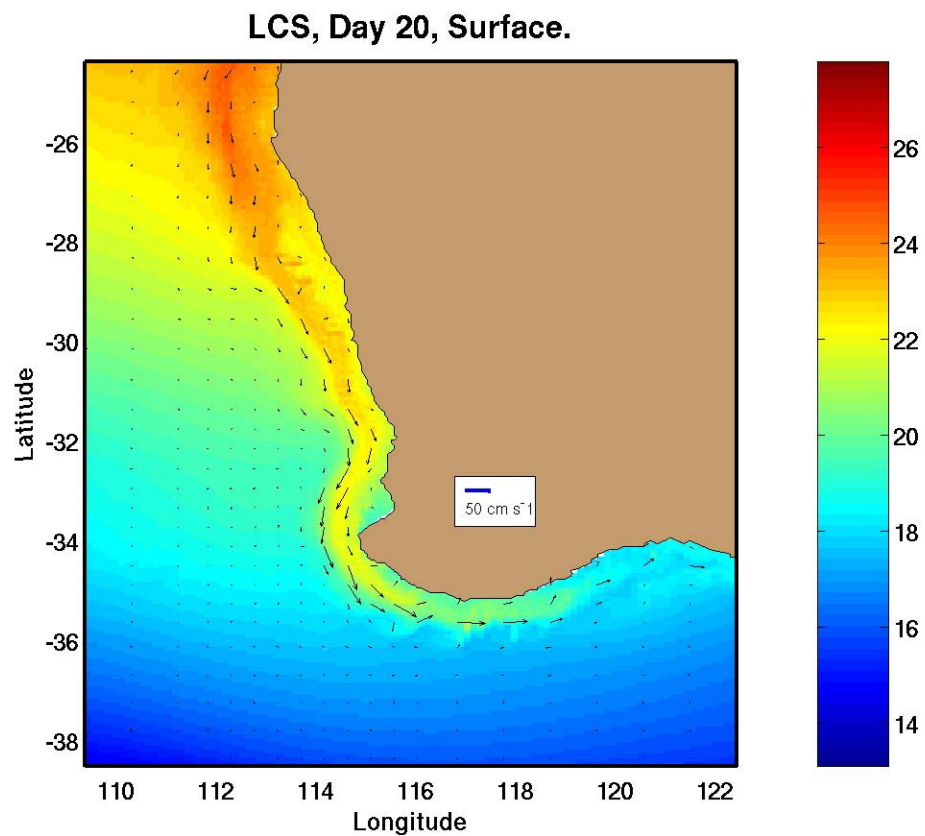


Figure 36. LCS, Surface temperature (°C) and velocity vectors (cm/s) on day 20.

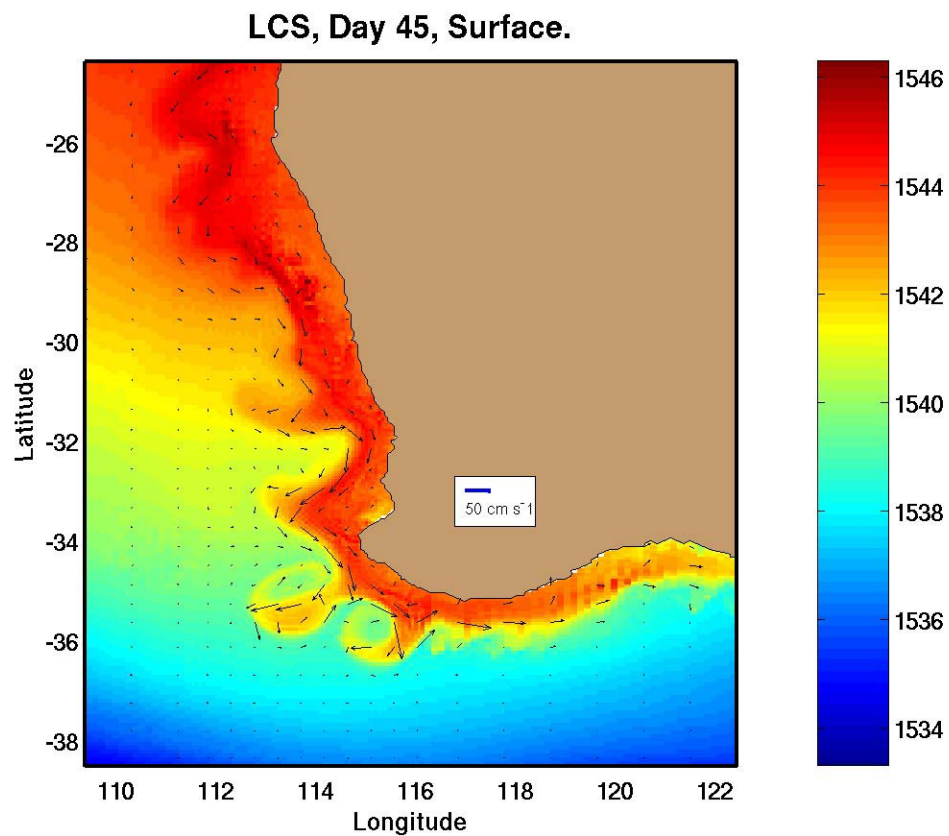


Figure 37. LCS, Surface sound speed (m/s) and velocity vectors on day 45.

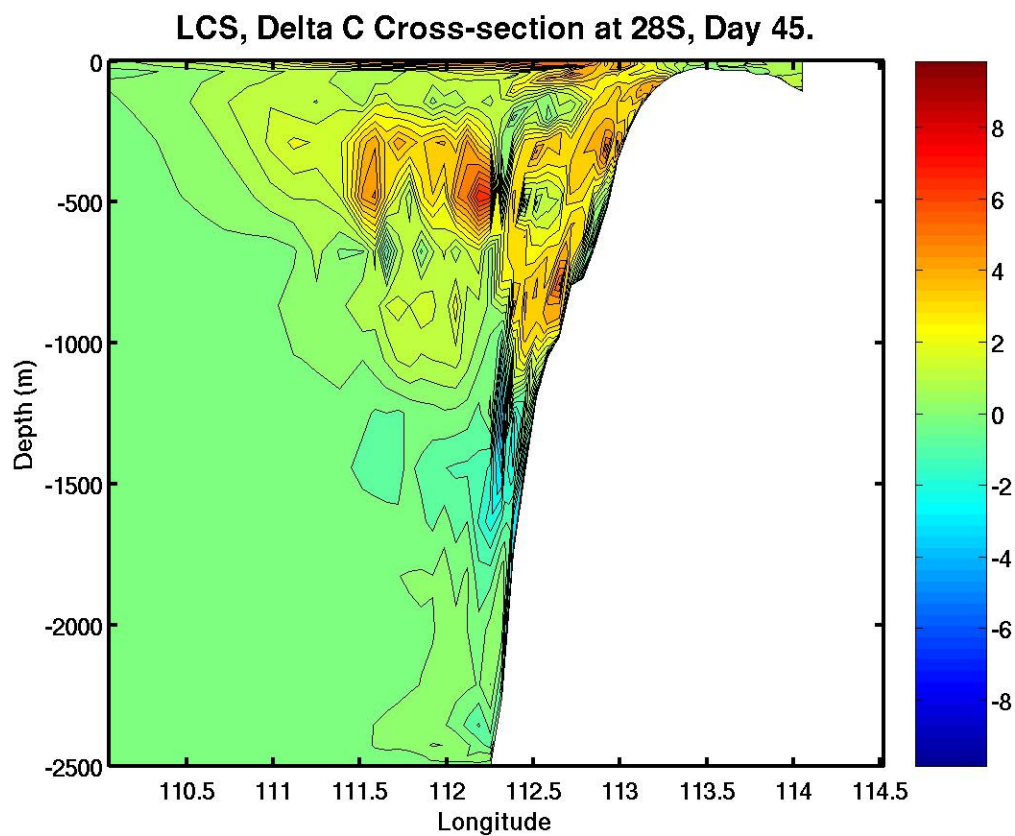


Figure 38. LCS, Difference in sound speed (m/s) from initial conditions, cross-section at 28°S on day 45.

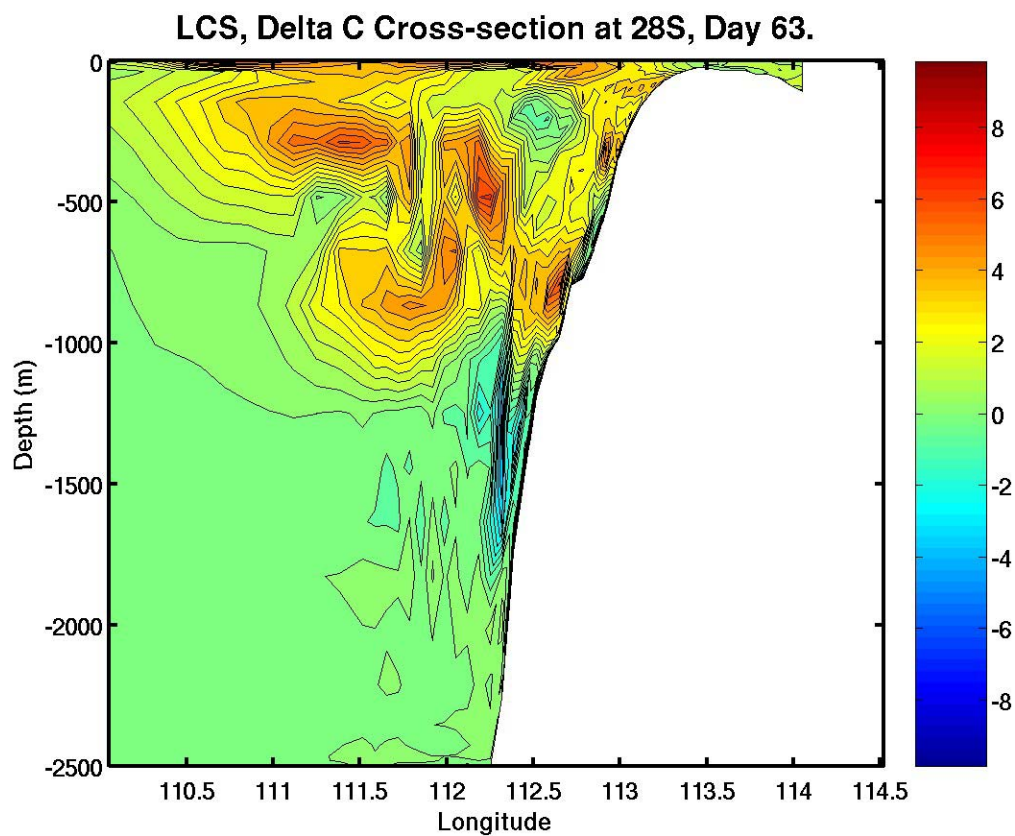


Figure 39. LCS, Difference in sound speed (m/s) from initial conditions, cross-section at 28°S on day 63.

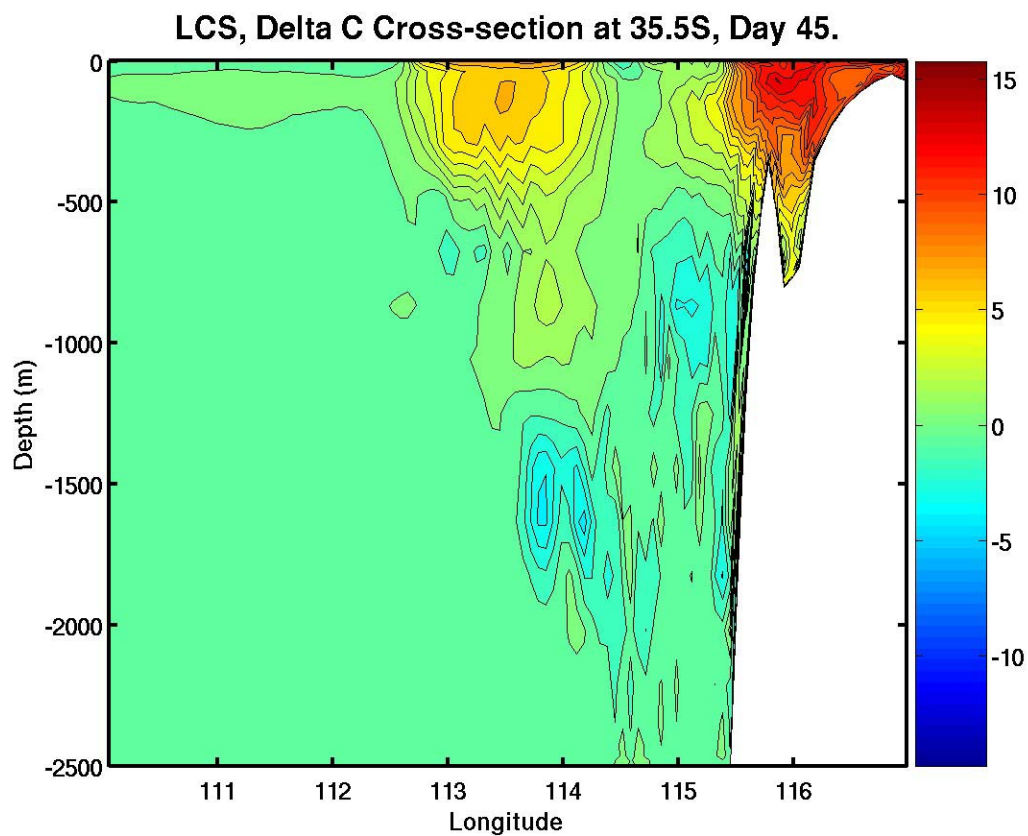


Figure 40. LCS, Difference in sound speed (m/s) from initial conditions, cross-section at 35.5°S on day 45.

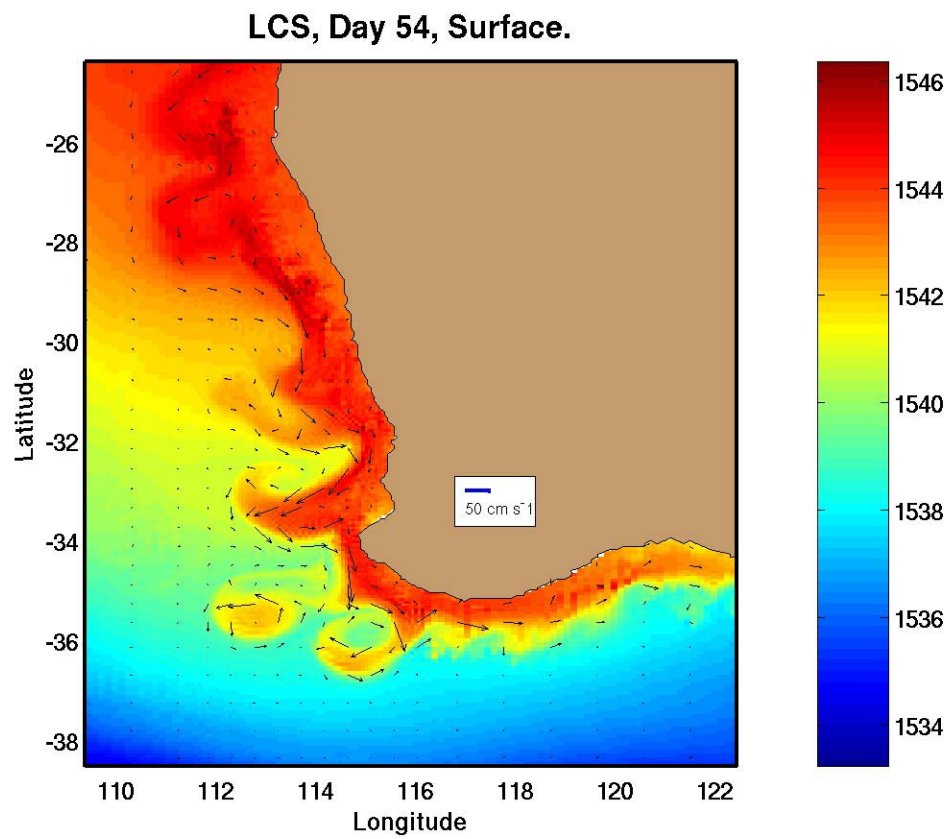


Figure 41. LCS, Surface sound speed (m/s) on day 54.

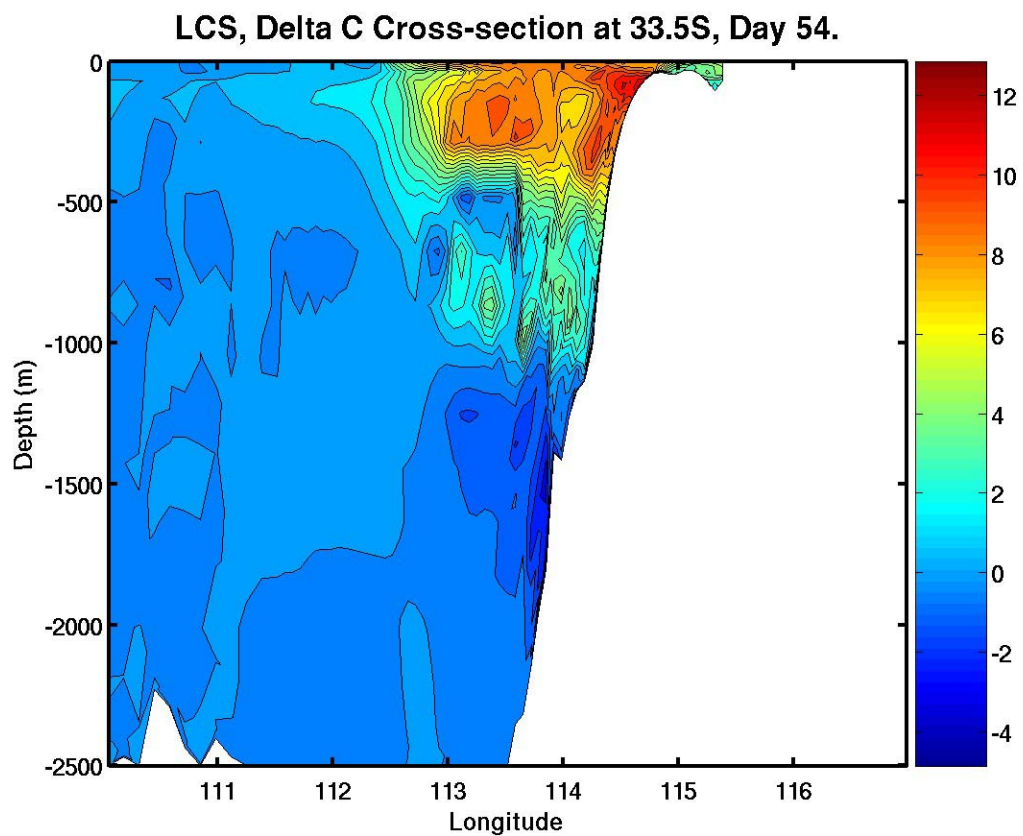


Figure 42. LCS, Difference in sound speed (m/s) from initial conditions, cross-section at 33.5°S on day 54.

Table 1. Vertical levels and depths used by Levitus and Boyer (1994) and Levitus et al. (1994).

Level	Depth (m)	Level	Depth (m)	Level	Depth (m)
1	0	12	300	23	1400
2	10	13	400	24	1500
3	20	14	500	25	1750
4	20	15	600	26	2000
5	50	16	700	27	2500
6	75	17	800	28	3000
7	100	18	900	29	3500
8	125	19	1000	30	4000
9	150	20	1100	31	4500
10	200	21	1200	32	5000
11	250	22	1300	33	5500

Table 2. Values of sigma levels for NCCS and LCS models.

Level	Sigma Value	Level	Sigma Value
1	0	12	-0.61538
2	-0.00961	13	-0.69231
3	-0.01923	14	-0.76923
4	-0.03846	15	-0.84615
5	-0.07692	16	-0.92308
6	-0.15385	17	-0.96154
7	-0.23077	18	-0.98077
8	-0.30769	19	-0.99038
9	-0.38462	20	-0.99519
10	-0.46154	21	-1.0
11	-0.53846		

Table 3. Impact of features on sound in the NCCS.

	Latitude	Δc	Lx	Lz
A. Maximum upwelling extension at day 63	39.3°N	-19 m/s	250 km	200 m
	36°N	-19 m/s	270 km	400 m
	32.5°N	-19 m/s	300 km	500 m
		Δc	Lx	Core depth
B. Undercurrent at day 36	39.3°N	+9 m/s	15 km	1600 m
	36°N	+5 m/s	20 km	1800 m
	32.5°N	+5 m/s	25 km	1500 m
	Day	Δc	Lx	Lz
C. Meddy at 39.3°N	45	+6 m/s	50 km	600 m
	63	+3.5 m/s	50 km	600 m
		Δc	Lx	
D. Eddy (undercurrent) at day 63		+ 2 m/s	100 km	
E. Eddy (surface) at day 63		-12.5 m/s	40 km	

Table 4. Impact of features on sound in the LCS.

A. Maximum upwelling extension at day 63	Latitude	Δc	Lx	Lz	
	28°S	+1 m/s	70 km	50 m	
	33.5°S	+4 m/s	40 km	50 m	
B. Surface current at day 36	Latitude	Δc	Lx	Lz	
	28°S	+5 m/s	200 km	1000 m	
	31.5°S	+9 m/s	120 km	700 m	
	33.5°S	+12 m/s	160 km	500 m	
C. Undercurrent at day 36	Latitude	Δc	Lx	Lz	Core Depth
	28°S	-3 m/s	25 km	500 m	1400 m
	31.5°S	-7 m/s	25 km	700 m	1200 m
	33.5°S	-4.5 m/s	30 km	800 m	1000 m
	35.5°S	-4 m/s	90 km	1000 m	1200 m
D. Eddy (surface)	Latitude	Δc	Lx	Lz	
	28°S	+7 m/s	250 km	1500 m	
	33.5°S	+10 m/s	180 km	400 m	
	35.5°S	+7 m/s	130 km	1200 m	
E. Eddy (undercurrent)	Latitude	Δc			
	28°S	0 m/s			
	33.5°S	-5 m/s			
	35.5°S	-2 m/s			

THIS PAGE INTENTIONALLY LEFT BLANK

LIST OF REFERENCES

- Ambar, I., A Shallow Core of Mediterranean Water off Western Portugal, *Deep-Sea Res.*, 30, 6A, 677-680, 1983.
- Ambar, I. and M.R. Howe. Observations of the Mediterranean Outflow – 1. Mixing in the Mediterranean Outflow. *Deep-Sea Res.*, 26, 535-554, 1979.
- Armi, L., D. Hebert, N. Oakey., J. F. Price, P. L. Richardson, H. T. Rossby, and B. Ruddick, Two Years in the Life of Mediterranean Salt Lens, *J. Phys. Oceanography*, 19, 354-370, 1989.
- Barton, E.D., Eastern Boundary of the North Atlantic: Northwest Africa and Iberia. *The Sea, Vol. 11, The Global Coastal Ocean: Regional Studies and Syntheses*, K.H. Brink and A.R. Robinson, eds., Wiley, New York, Chap.22, 633-657, 1998.
- Batteen, M. L., M. J. Rutherford, and E. J. Bayler, A Numerical Study of Wind and Thermal Forcing Effects on the Ocean Circulation Off Western Australia, *J. Phys. Oceanography*, 22, 1406-1433, 1992.
- Batteen, M. L., J. R. Martinez, D.W. Bryan, and E.J. Buch, A Modeling Study of the Coastal Eastern Boundary Current System off Iberia and Morocco, *J. Geophys. Res.*, 105 (C6), 14,173-14,195, 2000.
- Batteen, M. L., R. A. Kennedy, Jr. and H.A. Miller, A process-Oriented Numerical Study of Currents, Eddies and Meanders in the Leeuwin Current System, *Deep-Sea Res.*, Submitted, 2006.
- Bower, A., L. Armi, and I. Ambar, Lagrangian Observations of Meddy Formation During A Mediterranean Undercurrent Seeding Experiment, *J. Phys. Oceanography*, 27, 2545-2575, 1997.
- Chapman, D. C., Numerical Treatment of Cross-Shelf Open Boundaries in a Barotropic Coastal Ocean Model, *Journal of Phys. Oceanography*, 25, 1060-1075, 1985.
- Chen, C. T. and F. J. Millero, Speed of Sound in Seawater at High Pressures. *J. Acoust. Soc. Am.*, 32(10), p. 1357, 1977.
- Church, J. A., G. R. Cresswell, and J. S. Godfrey, The Leeuwin Current. In: *Poleward Flows Along Eastern Ocean Boundaries*, S. Neshyba, C. N. K. Moorers, R. I. Smith, and R. T. Barber, Eds., Springer-Verlag, 230-252, 1989.
- Cresswell, G. R. and T. J. Golding, Observations of a South-Flowing Current in the Southeastern Indian Ocean, *Deep-Sea Res.*, 27A, 449-466, 1980.
- Cresswell, G. R. and J. L. Peterson, The Leeuwin Current South of Western Australia, *Aust. J. Mar. Freshwater Res.*, 44, 285-303, 1993.

- Del Grosso, V. A., New equation for the speed of sound in natural waters (with comparisons to other equations), *J. Acoust. Soc. Am.*, 56(4), pp. 1084-1091, 1974.
- Dushaw, B. D., P. F. Worcester, B. D. Cornuelle, and B. M. Howe. On equations for the speed of sound in seawater. *J. Acoust. Soc. Am.*, 93, 255-275, 1993.
- Ezer, T. and G. L. Mellor, Diagnostic and Prognostic Calculations of the North Atlantic Circulation and Sea Level Using a Sigma Coordinate Ocean Model, *J. of Geophys. Res.*, 99(C7), 14159-14171, 1994.
- Ezer, T. and G. L. Mellor, Simulations of the Atlantic Ocean With a Free Surface Sigma Coordinate Ocean Model, *J. of Geophys. Res.*, 102(C7), 15647-15657, 1997.
- Fiuza, A. F. de G., The Portuguese Coastal Upwelling System, Actual problems of Oceanography in Portugal, Junta Nacional de Investigação Científica e Tecnológica, Lisboa, 45-71, 1980.
- Fiuza, A. F. de G., M. E. de Macedo, M. R. Guerreiro, Climatological Space and Time Variation of the Portuguese Coastal Upwelling, *Oceanológica Acta*, Vol. 5, No. 1, 31-40, 1982.
- Fiuza, A. F. de G., Hidrologia e Dinâmica das Aguas Costeiras de Portugal. Dissertação apresentada a Universidade de Lisboa para obtenção do grau de Doutor em Física, especialização em Ciencias Geofísicas. Univ. Lisboa, 294 pp., 1984.
- Fiuza, A. F. de G. and F. M. Sousa, Preliminary Results of a CTD Survey in the Coastal Transition Zone off Portugal Durin 1-9 September 1988, *Coastal Transition Zone Newsletter*, 4, 2-9, 1989.
- Fofonoff, P. and R. C. Millard, Algorithms for Computation of Fundamental Properties of Seawater, *Unesco Tech. Pap. In Mar. Sci.*, 44, 53, 1983.
- Frouin, R., A. F. G. Fiuza, I. Ambar, and T. J. Boyd, Observations of a Poleward Surface Current off the Coasts of Portugal and Spain during Winter, *J. Geophys. Res.*, 95, 679-691, 1990.
- Gentilli, J., *Australian climate patterns*, Nelson, Melbourne, 1972.
- Godfrey, J. S. and K. R. Ridgway, The Large-Scale Environment of the Poleward-Flowing Leeuwin Current, Western Australia: Longshore Steric Height Gradients, Wind Stresses and Geostrophic Flow, *J. Phys. Oceanography*, 15, 481-495, 1985.
- Godfrey, J. S., D. J. Vaudrey, and S. D. Hahn, Observations of the Self-Edge Current South of Australia Winter 1982, *J. Phys. Oceanography*, 16, 668-679, 1986.
- Hagen, E., C. Zulicke, and R. Feistel, Near-Surface Structures in the Cape Ghir Filament off Morocco, *Oceanol. Acta*, 19, 6, 577-598, 1996.

- Haynes, R. and E. D. Barton, A Poleward Flow Along the Atlantic Coast of the Iberian Peninsula, *J. Geophys. Res.*, 95, 11425-11441, 1990.
- Haynes, R., E. D. Barton, and I. Pilling, Development, Persistence and Variability of Upwelling Filaments off the Atlantic Coast of Iberia, *J. Geophys. Res.*, 98, 22681-22692, 1993.
- Hebert, D., N. Oakey, and B. Ruddick, Evolution of a Mediterranean Salt Lens: Scalar Properties, *J. Phys. Oceanography*, 20, 1468-1483, 1990.
- Hirst, A. C., and J. S. Godfrey, The role of Indonesian Throughflow in a Global Ocean GCM, *J. Phys. Oceanography*, 23, 1057-1086, 1993.
- Iorga, M. C., and M. S. Lozier, Signatures of the Mediterranean Outflow from a North Atlantic Climatology, 1. Salinity and Density Fields, *J. Geophys. Res.*, 104, 25985-26009, 1999.
- Legeckis, R. and G. Cresswell, Satellite observations of sea surface temperatures fronts off the coast of Western and Southern Australia, *Deep-Sea Res.*, 28(3A), 297-306, 1981.
- Levitus, S., and T. P. Boyer, World Ocean Atlas 1994, Vol. 4: Temperature, *NOAA Atlas NESDI 4*, 117 pp., U. S. Dept. of Commerce, Washington, D.C., 1994.
- Levitus, S., R. Burgett, and T. P. Boyer, World Ocean Atlas 1994, Vol. 3: Salinity, *NOAA Atlas NESDI 3*, 99 pp., U. S. Dept. of Commerce, Washington, D.C., 1994.
- Lurton, X., *An introduction to Underwater Acoustics*, Springer: Chichester, 2002.
- Marchesiello, P., J. C. McWilliams, and A. Shchepetkin, Open Boundary Conditions for Long-Term Integration of Regional Oceanic Models, *Ocean Modeling*, 3, 1-20, 2001.
- Martinho, A. S., A Fine Resolution Model of the Coastal Eastern Boundary Current Systems Off Iberia and Morocco, Master's Thesis, Naval Postgraduate School, Monterey, California, 93 pp, 2001.
- Martinho, A. S., On Reducing the Slope Parameter in Terrain-following Numerical Ocean Models, *Ocean Modelling*, 13, 166-175, 2006.
- McCreary, J. P., S. R. Shetye, and P. K. Kundu, Thermohaline Forcing of Eastern Boundary Currents: With Application to the Circulation Off the West Coast of Australia, *J. Mar. Res.*, 44, 71-92, 1986.
- Mellor, G. L., User's guide for a Three-Dimensional, Primitive Equation, Numerical Ocean Model, 40 pp, Program in Atmos. And Ocean Sci. Report, Princeton Univ., Princeton, NJ, 1996.
- Mellor, G. L., L. Y. Oey, and T. Ezer, Sigma Coordinate Pressure Gradient Errors and the Seamount Problem, *J. Atmospheric and Ocean Technology*, 15, 1122-1131, 1998.

Mellor, G. L., and T. Yamada, Development of a Turbulence Closure Model for Geophysical Fluid Problems, *Rev. Geophys. Space Phys.*, 20, 851-875, 1982.

Nelson, C. S., Wind Stress and Wind Stress Curl Over the California Current, NOAA Tech Rep. NMFS SSFR-714, U.S. Dept Commerce, 87 pp., 1977.

Palma, E. D., and R. P. Matano, On the Implementation of Passive Open Boundary Conditions for a General Circulation Model: the Barotropic Mode, *J. Geophys. Res.*, 103(C1), 1319-1341, 1998.

_____, On the Implementation of Open Boundary Conditions for a General Circulation Model: The three-dimensional case. *J. Geophys. Res.*, 105(C4), 8605-8627, 2000.

Parrish, R. H., A. Bakun, D. M. Husby, and C. S. Nelson, Comparative Climatology of Selected Environmental Processes in Relation to Eastern Boundary Current Pelagic Fish Reproduction. In: *Proc. Expert Consultation to Examine Changes in Abundance and Species of Neritic Fish Resources*,

Pearce, A. F. and R. W. Griffiths, The Mesoscale Structure of the Leeuwin Current: A Comparison of Laboratory Model and Satellite Images, *J. Geophys. Res.*, 96, 16739-16757, 1991.

Richardson, P. L., and A. Tychensky, Meddy trajectories in the Canary Basin measured during the SEMAPHORE experiment, 1993-1995. *J. Geophys. Res.*, 103, 25029-25045, 1998.

Sandwell, D. T., and W. F. Smith, Global Bathymetric Prediction for Ocean Modeling and Marine Geophysics, 1996.

Saunders, P. M., Practical Conversion of Pressure to Depth, *J. Phys. Oceanography*, 11, 573-574, 1981.

Smagorinsky, J., S. Manabe, and J. F. Holloway, Numerical Results From a Nine-Level General Circulation Model of the Atmosphere, *Mon. Weather Rev.*, 93, 727-768, 1965.

Smith, R. L., A. Huyer, J. S. Godfrey, and J. A. Church, The Leeuwin Current Off Western Australia, 1986-1987, *J. Phys. Oceanography*, 21, 323-345, 1991.

Stammer, D., H. H. Hinrichsen, and R. H. Kase, Can Meddies Be Detected By Satellited Altimetry?, *J. Geophys. Res.*, 96, 1005-7014, 1991.

Thompson, R. O. R. Y., Observations of the Leeuwin Current Off Western Australia, *J. Phys. Oceanography*, 14, 623-628, 1984.

Trenberth, K. E., W. G. Large, J. G. Olsen, The Mean Annual Cycle in Global Ocean Wind Stress, *J. Phys. Oceanography*, 20, 1742-1760, 1990.

Van Camp, L., L. Nykjaer, E. Mittelstaedt, and P. Schlittenhardt, Upwelling and Boundary Circulation off Northwest Africa as Depicted by Infrared and Visible Satellite Observations, *Prog. Oceanog.*, 26, 357-402, 1991.

Wilson W D, Equation for the Speed of Sound in Seawater. *J Acoust Soc Am*, 32(10), p 1357, 1960.

Wooster, W. S., and J. L. Reid Jr., Eastern boundary currents, in *The Seas*, Vol. 2, edited by M. N. Hill, pp. 253-280, John Wiley, New York, 1963.

THIS PAGE INTENTIONALLY LEFT BLANK

INITIAL DISTRIBUTION LIST

1. Defense Technical Information Center
Ft. Belvoir, Virginia
2. Dudley Knox Library
Naval Postgraduate School
Monterey, California
3. Chair, Department of Oceanography (Code OC/Bv)
Naval Postgraduate School
Monterey, California
4. Dr. Mary L Batteen (Code OC/Bv)
Naval Postgraduate School
Monterey, California
5. Dr. John A. Colosi
Naval Postgraduate School
Monterey, California
6. ENS Vanessa Guthrie
Naval Postgraduate School
Monterey, California
7. CDR Tony Miller
Naval Postgraduate School
Monterey, California
8. Dr. Don Brutzman
Naval Postgraduate School
Monterey, California
9. LT Alicia Hopkins
Naval Postgraduate School
Monterey, California
10. Dr. Hong Zhou
Naval Postgraduate School
Monterey, California